



1 Recent Precipitation Decrease Across the Western Greenland Ice Sheet 2 Percolation Zone

3 Lewis, Gabriel¹; Osterberg, Erich¹; Hawley, Robert¹; Marshall, Hans Peter²; Meehan, Tate²; Graeter, Karina³;
4 McCarthy, Forrest⁴; Overly, Thomas^{5,6}; Thundercloud, Zayta¹; Ferris, David¹

5 ¹Department of Earth Sciences, Dartmouth College, Hanover, NH, USA

6 ²Geosciences Department, Boise State University, Boise, ID, USA

7 ³Office of Sustainability, University of Maine, Orono, ME, USA

8 ⁴College of Fisheries and Ocean Sciences, University of Alaska Fairbanks, Fairbanks, AK, USA

9 ⁵NASA Cryospheric Sciences Laboratory, NASA Goddard Space Flight Center, Greenbelt, MD, USA

10 ⁶Earth System Science Interdisciplinary Center (ESSIC), University of Maryland, College Park, MD, USA

11 Correspondence to: Gabriel Lewis (Gabriel.M.Lewis.GR@dartmouth.edu)

12 Abstract

13 The mass balance of the Greenland Ice Sheet (GrIS) in a warming climate is of critical interest to scientists
14 and the general public in the context of future sea-level rise. Increased melting in the GrIS percolation zone
15 due to atmospheric warming over the past several decades has led to increased mass loss at lower elevations.
16 Previous studies have hypothesized that this warming is accompanied by a precipitation increase, as would
17 be expected from the Clausius-Clapeyron relationship, negating some of the melt-induced mass loss
18 throughout the Western GrIS. This study tests that hypothesis by calculating snow accumulation rates and
19 trends across the Western GrIS percolation zone, providing new critical accumulation estimates in regions
20 with sparse and/or dated *in situ* data for calibration of future regional climate models. We present
21 accumulation records from sixteen 22 – 32 m long firn cores and 4436 km of ground penetrating-radar,
22 covering the past 20 – 60 years of accumulation, collected across the Western GrIS percolation zone as part
23 of the Greenland Traverse for Accumulation and Climate Studies (GreenTrACS) project. Trends from both
24 radar and firn cores, as well as commonly used regional climate models, show decreasing accumulation and
25 precipitation over the 1996 – 2016 period, which we attribute to shifting storm-tracks related to stronger
26 atmospheric summer blocking over Greenland. Changes in atmospheric circulation over the past 20 years,
27 specifically anomalously high summertime blocking, have reduced GrIS surface mass balance through both
28 an increase in surface melting and a decrease in accumulation.

29 1. Introduction

30 Greenland Ice Sheet (GrIS) mass loss has accelerated over the past few decades, with modern mass loss rates
31 more than double that from Antarctica (van den Broeke et al., 2016). The 2010-2018 GrIS mass loss is 286
32 ± 20 Gt a⁻¹ (Mouginot et al., 2019), contributing 0.7 ± 0.2 mm a⁻¹ of sea level rise. Over the past 20 years, the
33 largest warming rates (Hanna et al., 2012) and fastest mass loss have occurred in Western Greenland (26 ± 7



34 GT a^{-2} in basins F + G of Sasgen et al., 2012), where surface mass balance (SMB) has decreased between
35 31.1% (European Centre for Medium Range Weather Forecasting downscaled; ECMWFd) and 76.5%
36 (Modèle Atmosphérique Régional; MAR) over the 1996 – 2008 period (Vernon et al., 2013) due to higher
37 surface melt and runoff (van den Broeke et al., 2009, 2016). Modern surface melt rates are at their highest
38 levels of at least the last 450 years across Western Greenland (Graeter et al., 2018) and more broadly
39 throughout Greenland (Trusel et al., 2018). In particular, ice core records from Western Greenland show an
40 abrupt increase in surface melt rates beginning in the middle-late 1990's due to a combination of higher North
41 Atlantic sea surface temperatures, enhanced summertime blocking highs, and anthropogenic warming
42 (Graeter et al., 2018).

43

44 Enhanced GrIS surface melt is driven fundamentally by rising Greenland temperatures as recorded by
45 automated weather stations from the Greenland Climate Network (GC-Net; Steffen and Box, 2001), coastal
46 weather stations (Box, 2002), borehole thermometry (Polashenski et al., 2014), remote sensing (Hall et al.,
47 2008), and ice core stable isotopes (Buchardt et al., 2012). Average annual temperature across interior
48 Greenland increased by $0.055 \pm 0.044 \text{ }^{\circ}\text{C a}^{-1}$ from 2000 – 2012 (Hall et al., 2013), with summer trends
49 upwards of $0.135 \pm 0.047 \text{ }^{\circ}\text{C a}^{-1}$ (Hall et al., 2013; Reeves Eyre and Zeng, 2017). These warming trends
50 extend to the highest elevations of the ice sheet, with warming at Summit Station of $0.09 \pm 0.01 \text{ }^{\circ}\text{C a}^{-1}$ from
51 1982 – 2011 (McGrath et al., 2013). Nearly every Greenland dataset shows statistically significant positive
52 temperature trends in recent decades, especially during the summers (Reeves Eyre and Zeng, 2017).

53

54 Basic physics implies that rising temperatures should cause an increase in accumulation over the ice sheet
55 due to the Clausius-Clapeyron relationship – warmer air has a higher saturation vapor pressure, potentially
56 leading to more precipitation (Box et al., 2006; Buchardt et al., 2012). The Coupled Model Intercomparison
57 Project, phase 5 (CMIP5) predicts precipitation increases of 20 – 50% over the GrIS by the end of the 21st
58 century (Bintanja and Selten, 2014), partially offsetting mass loss and sea-level rise from enhanced summer
59 melt and runoff. However, most *in situ* records of Greenland snow accumulation do not span the modern
60 period of rapid warming and accelerating mass loss since the mid-1990s. It is difficult to determine whether
61 accumulation has been increasing with the observed warming temperatures as predicted. For example, the
62 Program for Arctic Regional Climate Assessment (PARCA) campaign collected 46 shallow ice and firn cores
63 (<100 m long) and three deeper cores (120 – 152 m long) to capture the spatial and temporal accumulation
64 variability over the ice sheet (Mosley-Thompson et al., 2001). However, the PARCA firn cores were collected
65 in 1997 – 1998, just at the onset of accelerated surface melting (Graeter et al., 2018), and the precipitation
66 record from automated weather stations is too brief and localized to analyze significant precipitation trends
67 (Rennermalm et al., 2013). The most recently analyzed deep ice cores (over 100 m long) were collected in



68 2003 – 2004 (D4, D5, Sandy, Katie; Banta and McConnell, 2007) and there have been no published *in situ*
69 accumulation records from the Western GrIS percolation zone for the past decade. Updated *in situ* snow
70 accumulation data are needed from this region to assess recent changes in accumulation during this period of
71 warming and SMB loss from melt and runoff.

72

73 In addition to measuring snow accumulation with ice cores and automated snow depth sensors, several
74 previous studies have used ground-based and airborne radar to calculate GrIS accumulation and trends (e.g.
75 Medley et al., 2013; Spikes et al., 2004). For example, Hawley et al. (2014) found a 10% increase in northwest
76 coastal Greenland accumulation over the past 52 years using Ground Penetrating Radar (GPR) along the
77 Greenland Inland Traverse (GrIT; see Figure 1 for location), although they did not find any statistically
78 significant trends further inland between the North Greenland Eemian Ice Drilling (NEEM) site and Summit
79 Station. Similarly, Wong et al. (2015) show a coastal increase in precipitation near Thule over 1981 – 2012,
80 but no statistically significant change in precipitation rate further inland at the Camp Century, B26, or 2Barrel
81 ice core sites. Overly et al. (2016) found a 20% accumulation increase below 3000 m a.s.l. on the historic
82 Expéditions Glaciologiques Internationales au Groenland (EGIG) line from 1994 – 2004 vs. 1985 – 1994
83 using the Airborne SAR/Interferometric Radar Altimeter System (ASIRAS) radar. We build upon these
84 previous studies by collecting GPR data across the lower percolation zone of Western Greenland, where
85 airborne radargrams are often obscured by refrozen melt percolation (Nghiem et al., 2005). By having our
86 GPR antenna coupled with the snow, we avoid losing energy, and, therefore, penetration depth, from a strong
87 reflection off of the snow-air interface.

88

89 In addition to temperature-precipitation relationships through the Clausius-Clapeyron relationship, previous
90 studies have analyzed the dynamic climate controls on Greenland precipitation. Mernild et al. (2014), Auger
91 et al. (2017), and Lewis et al. (2017) have hypothesized that a positive Atlantic Multidecadal Oscillation
92 (AMO) index correlates with rising accumulation over most of the GrIS interior, since higher sea surface
93 temperatures increase moisture flux over the GrIS and induce greater snowfall. High pressure (blocking)
94 systems east of Greenland tend to deflect eastward-moving storms over central Greenland and increase
95 precipitation, whereas blocking directly over Greenland or in Baffin Bay has the potential to prevent storms
96 from crossing the ice sheet (Auger et al., 2017). Through reanalysis data, Auger et al. (2017) showed that
97 persistent blocking highs increase precipitation in southwest Greenland and reduce precipitation in the
98 southeast.

99

100 The Greenland Blocking Index (GBI) quantifies blocking directly over Greenland and is defined as the mean
101 500 hPa geopotential height for the 60 – 80°N, 20 – 80°W region (Hanna et al., 2016). Over the 1991 – 2015

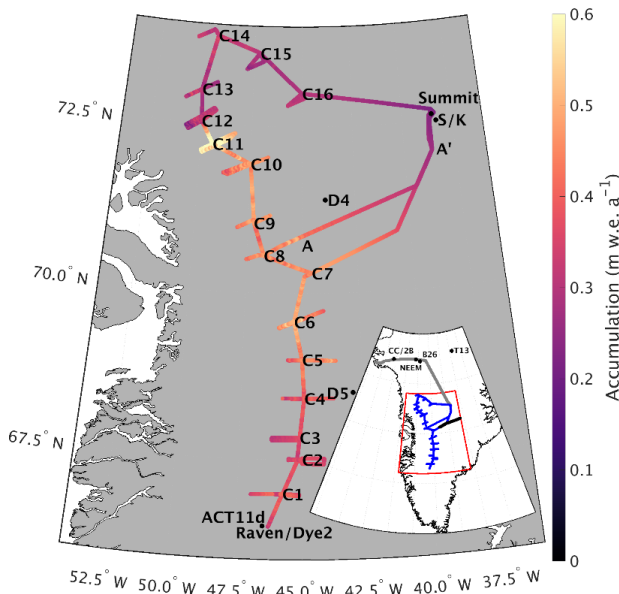


102 period there has been an especially high Greenland Blocking Index sustained throughout the summers (Hanna
103 et al., 2016). Alternatively, persistent blocking episodes have the potential to reduce snowfall accumulation
104 over the GrIS by displacing the polar jet stream and corresponding storm tracks equatorward, although this
105 relationship has not yet been documented *in situ*.

106

107 Here we develop new accumulation records across the Western GrIS percolation zone using sixteen firn cores
108 and 4436 km of GPR data collected during an over-ice traverse spanning two field seasons. We evaluate the
109 veracity of the accumulation data through comparisons of our firn core time series with previous
110 measurements. We quantify multi-year trends in accumulation across Western Greenland to test the
111 hypothesis that precipitation has recently increased from the Clausius-Clapeyron relationship and higher GrIS
112 temperatures. Further, we assess the ability of RCMs to capture the year-to-year variability and multi-year
113 trends in Western GrIS accumulation. Finally, we evaluate relationships between recent accumulation trends
114 and atmospheric circulation patterns, particularly changes in storm tracks.

115



116

117 **Figure 1.** Average accumulation across the GreenTrACS traverse for the length of each record showing the location of each firn core,
118 ACT11d, D4, D5, Katie (K), Raven/Dye-2, and Sandy (S) ice cores, and Summit Station. Transect A-A' discussed in Section 3.3. Inset
119 shows locations of Camp Century (CC), 2Barrel (2B), NEEM, B26, and TUNU2013 (T13) ice cores, as well as locations of EGIG (black),
120 GrIT (grey), and GreenTrACS (blue) traverses.

121 2. Methods

122 This study uses data from the 2016 – 2017 Greenland Traverse for Accumulation and Climate Studies
123 (GreenTrACS), which measured accumulation and melt across the Western GrIS percolation zone over two



124 summer snowmobile traverses (closely following the 2150 m a.s.l. elevation contour). The May-June 2016
125 season traversed 860 km from Raven/Dye-2 northward to Summit Station and the May – June 2017 traverse
126 made a 1230 km clockwise loop starting and ending at Summit Station (Figure 1). This manuscript focuses
127 on accumulation rates derived from 400 MHz GPR data collected along the entire traverse path, as well as
128 sixteen shallow (22 – 32 m long) firn cores spaced 40 – 100 km apart along the backbone of the traverse
129 (Figure 1). Firn Cores 1 – 7 were collected in 2016 and Cores 8 – 16 were collected in 2017. We returned to
130 the Core 7 location at the beginning of the 2017 traverse to recover a weather station and to connect the two
131 season’s GPR data. Additionally, we collected GPR data ~30 – 70 km east and west of each core site,
132 hereafter called “spurs”, to measure accumulation changes along strong elevation gradients (see Figure 1).

133 2.1. GPS Positioning

134 During the 2016 traverse we collected GPS data using a Trimble NetR8 reference receiver with a Zephyr
135 Geodetic antenna mounted to a Nansen sled ~5 m in front of the GPR antenna. For each spur and the tail
136 ends of each transect between core sites we performed differential corrections to the GPS data using RTKLIB
137 2.4.1 and a Trimble NetR8 base station near the core site. Between spurs, when not operating a base station,
138 we post-processed GPS data in precise point positioning mode (Zumberge et al., 1997). Estimated root-mean-
139 square horizontal errors were generally between 13 and 18 cm from standard deviations calculated during
140 stationary periods at the end of spurs. To co-register GPR and GPS data, we used time stamps embedded in
141 the two data streams and locations where we stopped to save GPR files, approximately every 15 km. The
142 time drift in the GPR logger is negligible over these durations.

143

144 During the 2017 traverse we used GPS data from a Garmin 19x GPS receiver wired directly to the GPR
145 instrument, which recorded position data at every radar sample with RMS values of 3 m. During radar
146 processing we average 75 adjacent traces, corresponding to a distance of ~20 m, so errors in GPS positioning
147 have a negligible effect on the final dataset.

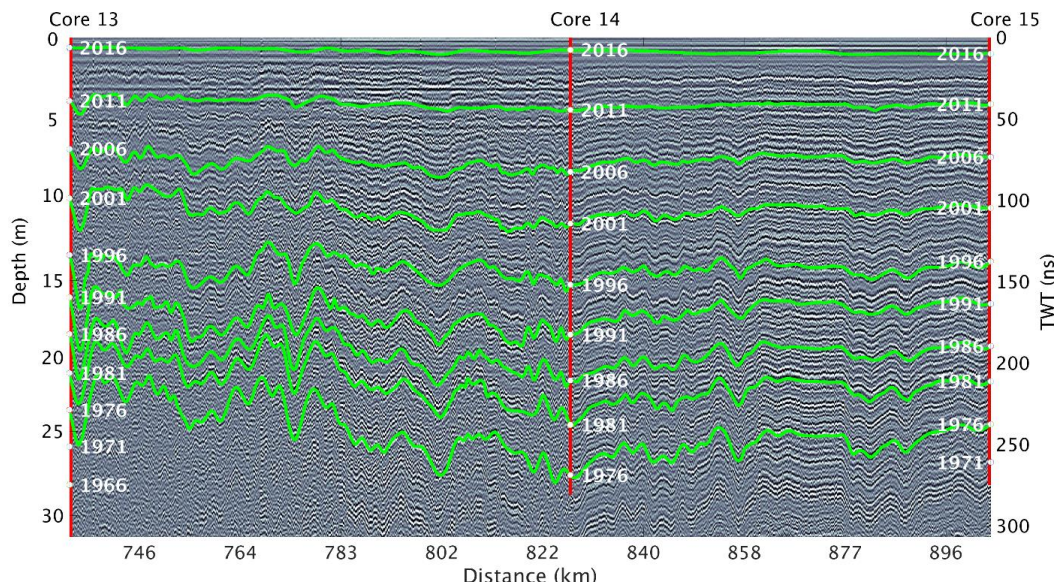
148

149 2.2. Ground-penetrating radar

150 We develop a spatially continuous record of accumulation using GPR profiles collected with Geophysical
151 Survey Systems Inc. (GSSI) SIR-3000 (during 2016) and SIR-30 (during 2017) radar units with a 400 MHz
152 antenna (following Hawley et al., 2014). The antenna was towed on the snow surface in a small plastic sled
153 ~5 m behind a wooden Nansen sled and ~15 m behind a snow machine. We recorded 2048 samples (2016)
154 and 4096 samples (2017) per trace over a range window of 800 ns (Figure 2). At a relative permittivity of
155 1.26 ± 0.07 , typical of firn in the GrIS percolation zone, the range was ~111 – 114 m. The 400 MHz short-



156 pulse radar has a range resolution (ability to resolve distinct features) of 0.35 ± 0.1 m in firn, which is fine
157 enough to resolve Internal Reflecting Horizons (IRHs) that have been shown to represent isochrones (Medley
158 et al., 2013; Rodriguez-Morales et al., 2014; Spikes et al., 2004; Hawley et al., 2014). We recorded 10 traces
159 per second, which at the snowmobile's average travel speed of approximately 2.75 m s⁻¹ results in ~3.6 traces
160 recorded per meter. Note that this spacing between traces varies with vehicle speed.



161

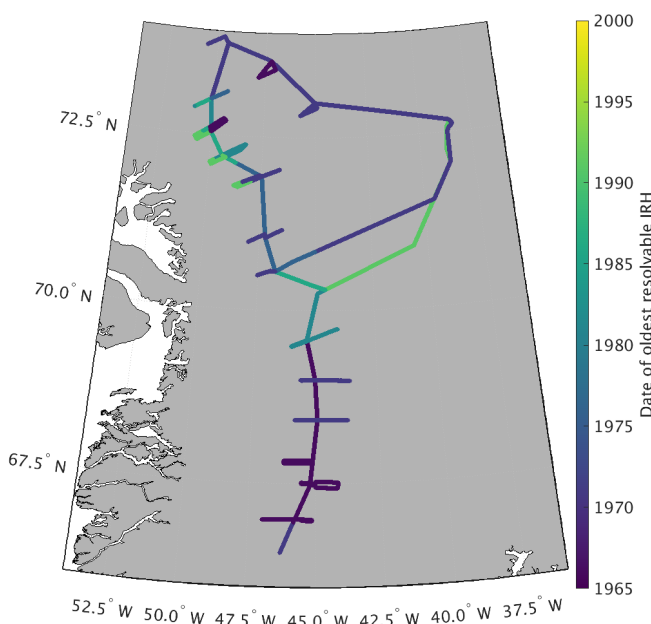
162 **Figure 2.** Radargram showing the top 32 m of the transect along the main 2017 traverse from Core 13 to Core 15. Cores are indicated as
163 red lines down to their final depth, with dates plotted every 5 years at corresponding depths. Traced internal reflecting horizons are
164 shown as isochronous green lines. The depth scale on the vertical axis is calculated from the TWT-depth conversion (see Section 2.4) for
165 Core 13, although there is no visual difference in depth scale across this radargram.

166 Depending on signal attenuation within the firn column, IRHs can be traced to a depth of 20 – 50 m (Figure
167 2), providing accumulation records over the past 20 – 60 years (Figure 3). For areas with high attenuation
168 (i.e. shallow penetration of the radar signal), such as lower elevation regions with more refrozen melt layers,
169 we calculate accumulation results for shorter time periods. We are not able to trace as many IRHs to the west
170 of Cores 10 – 13 compared to the east due to higher signal attenuation, resulting in slightly different average
171 accumulation values on either side of these cores (Figure 3). Likewise, we experienced an equipment
172 malfunction at the end of the 2016 traverse, reducing the number of observable IRHs from Core 7 to Summit
173 Station (Figure 3). We have less confidence in calculated accumulation throughout this section of the traverse
174 due to this malfunction, although the 2017 Summit to Core 8 interval overlaps nicely with the last 140 km of
175 the problematic 2016 interval, and provides high quality accumulation measurements for this section near
176 Summit Station.

177



178 We reduce the GPR data volume and signal noise by averaging 75 adjacent traces, which has the effect of
179 suppressing random noise by the principle of trace stacking (Yilmaz, 2001). We apply a combination of
180 median trace filtering, residual mean filtering (Gerlitz et al., 1993), and bandpass filtering using a butterworth
181 design (Selesnick and Sidney Burrus, 1998) between 200 – 800 MHz. For data visualization, we apply an
182 automatic gain control (Yilmaz, 2001) to give the interpreter more confidence when picking IRHs.
183
184



185
186 **Figure 3: Date of oldest resolvable internal reflecting horizon throughout the entire GreenTrACS traverse route. Anomalously young**
187 **ages from Core 7 to Summit are due to equipment malfunction.**

188

189 **2.3. Firn core processing and density profiles**

190 The amount of snow mass and the time span between IRHs are necessary to calculate accumulation rates.
191 The accumulation rate is a function of the depth-age scale, travel time-depth conversion rate, and the firn
192 density profile. We obtain the depth-age and depth-density scales from each of the shallow firn cores
193 collected along the GreenTrACS traverse, and from density models based on temperature and accumulation
194 rate data.

195

196 The sixteen firn cores were drilled using an Ice Drilling Program hand auger with a Kyne sidewinder
197 attachment (see Graeter et al., 2018). We sampled the firn cores for chemical measurements using a



198 continuous ice core melter system with discrete sampling (Osterberg et al., 2006). We used an Abakus (Klotz)
199 laser particle detector to measure microparticle concentrations and size distribution from the continuous ice
200 core meltwater stream, a Dionex Model ICS5000 capillary ion chromatograph to measure major ion (Na^+ ,
201 Mg^{2+} , Ca^{2+} , K^+ , NH_4^+ , Cl^- , NO_3^- , SO_4^{2-}) and methanesulfonic acid concentrations, and a Picarro L1102-I and
202 a Los Gatos Research Liquid Water Isotope Analyzer to measure oxygen and hydrogen isotope ratios ($\delta^{18}\text{O}$,
203 δD ; Graeter et al., 2018).

204

227 We determine depth-age curves for each core by identifying annual layers based on seasonal oscillations in
228 $\delta^{18}\text{O}$ and the concentrations of major ions and dust, consistent with previous ice core studies in this region
229 (Graeter et al., 2018; Mosley-Thompson et al., 2001; Osterberg et al., 2015). We combine the depth-age
230 scales with measured density to calculate annual accumulation rates at the firn core sites.

231

232 At each firn core and at the ends of each spur, we measured the density in the top meter of snow using a 1000
233 cm^3 SnowMetrics cutter. To calculate firn core density profiles, we measured the mass, length, and diameter
234 of 0.03–1 m long core segments in the field and again after transporting the cores to the Dartmouth College
235 Ice Core Laboratory. To calculate accumulation rates at Raven/Dye-2, we use density data from a 119.6 m
236 long firn core collected in 1997 (Bales et al., 2009) and a 19.3 m long core collected from the same location
237 in 2015, which did not include accumulation data (Vandecrux et al., 2018). For this location we use the most
238 recent density data for the near-surface and the older densities for depths below the 2015 core. Likewise, we
239 use a density profile from a 109 m long firn core collected from Summit in 2010 (Mary Albert, personal
240 communication, 2015). We also incorporate density data from measurements along the EIGI traverse at T19,
241 T21, T23, T27, and T31 to improve the density profile between Core 7 and Summit (Morris and Wingham,
242 2014).

243

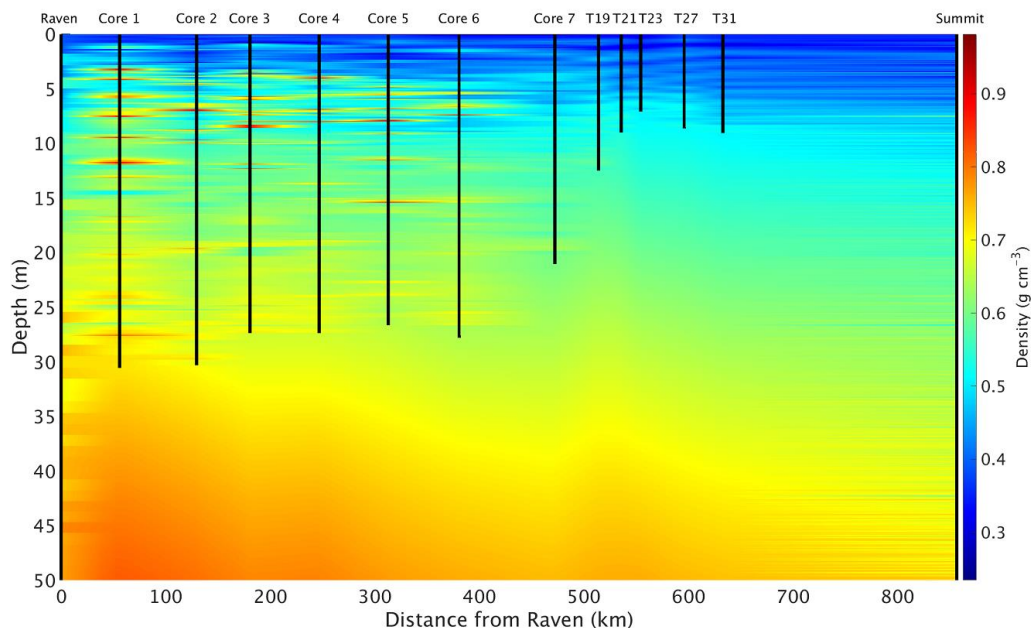
244 After collecting each firn core, we measured borehole temperature for 24 – 48 hours using a 20 m long
245 thermistor string. We estimate mean annual temperature from the deepest thermistor on the twenty-
246 thermistor-string. For the location of each firn core, we use the depth-density data from that core and then
247 calculate a Herron and Langway (1980) depth-density model for depths below the core using our measured
248 mean annual temperature, firn core mean annual accumulation, and top-meter snow density. Likewise, we
249 calculate Herron-Langway profiles for the ends of each spur using MODIS satellite derived mean annual
250 temperature (Hall et al., 2012), MAR modeled accumulation (Burgess et al., 2010), and the measured snow
251 density in the upper meter of each of the spur's snow pits. Finally, we interpolate depth-density profiles both
252 between firn cores and along radar spurs to estimate the depth-density matrix everywhere along our traverse



253 (Figure 4). Final accumulation rates are insensitive to the accumulation we use to calculate our Herron-
 254 Langway models (Lewis et al., 2017).

255

256 As shown in Figure 4, ice layers within several firn cores are extrapolated laterally along the traverse,
 257 although these dense lenses are typically both localized and heterogeneous in nature (Brown et al., 2011;
 258 Rennermalm et al., 2013). This ice lens density interpolation is as accurate as possible between firn cores
 259 without additional *in situ* data, and this estimation does not significantly alter our results, as discussed in
 260 Section 2.6, since the ice layers represent a small fraction of the total depth to IRHs.



261

262 **Figure 4.** Depth-density profile along the main 2016 traverse used for calculation of electromagnetic wave velocity and accumulation in
 263 this study. Densities are linearly interpolated between the two nearest cores and are modeled using Herron-Langway profiles below the
 264 depth of each core. The left and right boundary data come from the Raven/Dye-2 and Summit firn cores, respectively. Ice layers in Cores
 265 1–5 are clearly visible as red lenses, but their extent is, in reality, likely more localized.

266

267 2.4. Travel-time to depth conversion

268 We convert the radar travel time to depth by iteratively multiplying the velocity of the electromagnetic wave
 269 by the signal's one-way travel time to each IRH. The electromagnetic speed of the radar wave, v (m s^{-1}), is
 270 calculated from the dielectric permittivity, ϵ_r (dimensionless), and the speed of light in a vacuum, c ($3 \times 10^8 \text{ m s}^{-1}$), from
 271

$$272 v = \frac{c}{\sqrt{\epsilon_r}} \quad (1).$$



273 In turn, we calculate the dielectric permittivity for each radar trace from the density, ρ (g cm^{-3}), of snow and
274 ice at depth, as shown in Figure 4, for each radar trace at every range bin (following Kovacs et al., 1995) by
275 $\epsilon_r = (1.0 + 0.845 * \rho)^2$ (2).

276 We calculate the depth of each subsequent radar sample for each trace in the profile using the radar travel
277 time and velocity profile from equations 1 and 2, following Hawley et al. (2014) and Lewis et al. (2017).

278

279 **2.5. Internal reflecting horizons**

280 We manually select 10 clear, strong IRHs spaced approximately 5 years apart to consistently trace from
281 Raven/Dye-2 to Summit Station and throughout the 2017 main traverse (Figure 2). We trace each layer
282 manually by visually identifying strong amplitude peaks throughout the radargram, starting with the 2016
283 layer and working downwards. We use a spline interpolation between manual picks to trace each layer along
284 large amplitude reflections every $\sim 500 - 700$ m along the traverse. When a layer appears to bifurcate due to
285 changes in accumulation, we continue to trace the layer based on the trajectory of surrounding IRHs.
286 Horizons are not traced in areas where the attenuated signal makes them too difficult to interpret (Figure 3).
287 We trace layers for each spur starting at the depth of each layer at the corresponding firn core location. We
288 can trace layers below the depth of some firn cores by tracing them from cores that are deeper or have lower
289 accumulation rates.

290

291 We trace layers between cores using a connect-the-dots approach using the depth-age scale at each firn core.
292 We trace layers from one firn core to the next before checking that we intersect that core location at the
293 proper depth for the age of our traced IRH. Note that the depths of several layers at Cores 2 – 16 are located
294 below the bottom depth of those cores. Since these layers are isochronous, they are used to calculate
295 accumulation over appropriate time epochs by using dates obtained from intersections with other cores (see
296 Figure 3).

297

298 **2.6. Accumulation calculations and uncertainty**

299 Finally, we calculate snow accumulation using the firn core depth-age scales, measured and interpolated
300 depth-density profiles (Figure 4), and traced IRHs (Figure 2). We calculate the water equivalent accumulation
301 \dot{b} (m w.e. a^{-1}) between adjacent IRHs from the depth z (m) and age t (year) of each layer, the average density
302 ρ (kg m^{-3}) between layers, and the density of water ρ_w (1000 kg m^{-3}):

$$303 \dot{b} = \frac{1}{t_2 - t_1} \int_{z_1}^{z_2} \frac{\rho(z)}{\rho_w} dz \quad (3)$$



304

305 We correct for layer thinning using a Nye (1963) model. The thinning factor has an average value of 0.9993
306 ± 0.0003 and is multiplied by the accumulation rate for each radar trace. For each radar trace, the thinning
307 factor, $\lambda(z)$, is calculated from the average accumulation \dot{b} (m w.e. a^{-1}) of each epoch, average age of the
308 epoch a (year), and water equivalent thickness of the GrIS H (m), from Morlighem et al. (2014):

309
$$\lambda(z) = e^{-\frac{b}{H}a} \quad (4).$$

310

311 Accumulation uncertainty can arise from independent errors in tracing IRHs, errors from incorrectly dating
312 firn cores, and/or errors in the densities used for converting from separation distance to water equivalent
313 accumulation. To reduce tracing errors, we retraced each IRH along the two main traverse paths four times
314 each. Close inspection of the IRHs reveals that the peaks defining IRHs are within ± 2 radar samples (within
315 at most ± 0.12 m), and incorrectly jumping to the next IRH would result in an error of at most ± 10 samples
316 (within ± 0.55 m). Our average epoch between IRHs is 5.0 years from the firn core depth-age scales, which
317 corresponds to a maximum tracing error of $\sim \pm 0.11$ m a^{-1} for each epoch, or a maximum error of ± 0.061 m
318 w.e a^{-1} , for an average density of 0.55 g cm $^{-3}$ over this dataset.

319

320 We perform a leave-one-out cross validation to calculate accumulation errors at locations where we do not
321 have firn core density profiles. Here we choose one of the sixteen firn cores, in addition to the Raven/Dye-2
322 and Summit cores, to omit from our density interpolation (Figure 4), so that we interpolate density profiles
323 between adjacent firn cores and a Herron-Langway profile at the missing core location. We find maximum
324 single-epoch errors of 0.079 m w.e. a^{-1} and maximum RMS (1971 – 2016) errors of 0.046 m w.e. a^{-1} (Table
325 1) at the location of missing cores, corresponding to 20.1% of the accumulation at that location. These
326 differences are approximately twice as large at Cores 1 – 6 than Cores 7 – 16 due to larger differences between
327 measured and interpolated density profiles, likely a result of meltwater percolation and ice lenses (Graeter et
328 al., 2018).

329

330 Similarly, we perform a leave-out-out validation by omitting a firn core density profile location entirely and
331 interpolating density profiles over a larger distance (e.g. between Core 1 and Core 3). In this case we find
332 maximum single-epoch errors of 0.057 m w.e. a^{-1} and maximum RMS (1971 – 2016) errors of 0.033 m w.e.
333 a^{-1} .

334

335 We conservatively take our accumulation error from missing density measurements to be 0.079 m w.e. a^{-1} .
336 This error highlights the importance of our firn core spacing between 40 – 100 km along the traverse and



337 confirms that the accuracy of future remotely sensed radar accumulation (e.g. IceBridge snow and
338 accumulation radars) estimates depend on precise field-based *in situ* density profiles for accurate
339 accumulation history in the percolation zone. Overly et al. (2016) calculated accumulation in the dry snow
340 zone using Herron-Langway profiles within 3.5% of accumulation calculated using neutron-probe density
341 profiles. However, here we show that *in situ* measurements, or accurate meltwater percolation modeling
342 (Meyer and Hewitt, 2017), are required to correctly calculate SMB in the percolation zone.
343

344 **Table 1.** Difference between accumulation rates at each GreenTrACS core site calculated using Herron-Langway profiles and firn core
345 density information.

Core	RMS average difference (m w.e. a^{-1})	Max epoch difference (m w.e. a^{-1})	Max Epoch difference (% of acc.)
1	0.046	0.079	20.1
2	0.025	0.061	16.2
3	0.037	0.074	19.9
4	0.028	0.045	10.7
5	0.026	0.054	11.5
6	0.038	0.052	10.0
7	0.015	0.026	5.4
8	0.026	0.045	10.3
9	0.030	0.049	10.9
10	0.019	0.039	8.5
11	0.023	0.035	5.0
12	0.018	0.027	8.2
13	0.025	0.031	10.7
14	0.019	0.027	8.2
15	0.010	0.016	5.3
16	0.014	0.025	8.2

346
347 We assume uncertainty in dating the firn cores from annual layer counting to be ± 0.5 years (Buchardt et al.,
348 2012). At the lowest accumulation locations, the smallest distance between layers is 0.15 m w.e. over an
349 epoch of 4.91 years. This gives an uncertainty in accumulation due to dating of at most $\sim \pm 0.03$ m w.e. a^{-1} .
350 The error associated with measuring *in situ* firn density has been estimated to be 1.4% (Karlöf et al., 2005).
351 However, following Hawley et al. (2014) and Lewis et al. (2017), we conservatively assume that our
352 measurements have a density measurement error of up to twice this large, corresponding to a maximum
353 accumulation error of ± 0.014 m w.e. a^{-1} .

354
355 We calculate the total uncertainty from formal error propagation (following Bevington and Robinson, 1992)
356 from the average accumulation rate $\dot{b} = 0.385$ m w.e. a^{-1} , average thickness between IRHs $\Delta h = 3.56$,



357 uncertainty in tracing δh , average firn density ρ , uncertainty in density measurements $\delta\rho$, average time
358 period between IRHs Δt , and uncertainty in core dating δt . We find a total accumulation rate uncertainty of
359 0.0709 m w.e. a^{-1} from equation 5.

$$360 \quad \sigma_b = \sqrt{b^2 \left(\left(\frac{\delta h}{\Delta h} \right)^2 + \left(\frac{\delta t}{\Delta t} \right)^2 + \left(\frac{\delta \rho}{\rho} \right)^2 \right)} \quad (5)$$

361

362 Due to the random and non-systematic nature of these errors, we can assume that they are unlikely to
363 contribute to a regional or temporal accumulation bias. To calculate uncertainty for accumulation averaged
364 over multiple epochs ($\sigma_{n-epochs}$) we divide our uncertainty σ_{epoch} by the square root of the number of traced
365 layers (n) at that location.

$$366 \quad \sigma_{n-epochs} = \frac{\sigma_{epoch}}{\sqrt{n}} \quad (6).$$

367

368 2.7. Model comparison

369 We compare our GreenTrACS accumulation results with annual outputs from Box et al. (2013; hereafter
370 “Box13”; 1840 – 1999), the Fifth Generation Mesoscale Model (Polar MM5; 1958 – 2008; Burgess et al.,
371 2010), MAR (1948 – 2015; Fettweis et al., 2016), and the Regional Atmospheric Climate Model (RACMO2;
372 1958 – 2015; Noël et al., 2018) over common time periods. Grid cell sizes for these model outputs are 5 km,
373 3 km, 5 km, and 1 km, respectively. For each radar trace we calculate statistically significant differences (at
374 $\alpha = 0.05$) using a two sample t-test with the GreenTrACS accumulation records for each epoch and RCM
375 accumulation for each common year. Additionally, we compare our GreenTrACS accumulation with an
376 accumulation map kriged from 295 firn cores and 20 coastal weather stations (Bales et al., 2009; hereafter
377 “Bales09”). We perform the same two sample t-test with the reported Bales09 uncertainty of 0.092 m w.e. a^{-1}
378 ¹ (Bales et al., 2009).

379

380 2.8. Accumulation trends

381 To investigate recent changes in GrIS accumulation, we calculate trends in accumulation across our GPR and
382 GreenTrACS firn core dataset. We fit a linear model to the accumulation time series for each radar trace and
383 analyze the trend for both slope and statistical significance. Likewise, we calculate trends and their statistical
384 significance for total precipitation (snowfall + rainfall) for MAR and RACMO2 grid cells from 1996 through
385 the end of both models’ temporal coverage. We can compare these results with our accumulation trends since
386 precipitation and accumulation are nearly identical above the equilibrium line altitude, due to zero runoff and
387 negligible sublimation within the percolation zone.



388 **2.9. Storm track changes**

389 To investigate the potential role of changing storm tracks in precipitation changes over the Western GrIS, we
390 utilize the updated Serreze (2009) storm track database. This database contains six-hour interval positions of
391 extratropical cyclone storm centers on a 2.5° grid. These centers are defined when a gridpoint sea level
392 pressure is surrounded by gridpoints at least 2 mb higher than the central point (Serreze, 2009). We calculate
393 the total number of days in which a storm center is located within our region of interest for each season. To
394 determine statistical significance, we run a two sample t-test on the number of storms in our region of interest
395 between 1958 – 1996 compared with 1996 – 2016.

396 **3. Results and discussion**

397 **3.1. Firn core and GPR accumulation records**

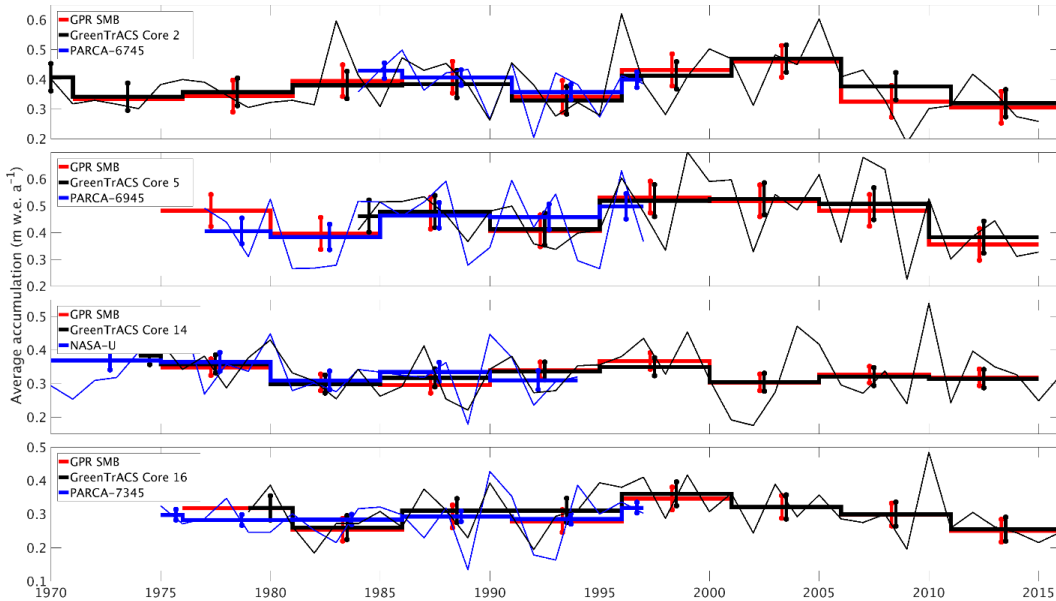
398 Figure 1 displays the mean accumulation at each location along the traverse route, with higher accumulation
399 rates in the southwest and lower accumulation rates at higher elevations of the ice sheet interior, broadly
400 consistent with previously published accumulation compilations (e.g. Bales et al., 2009) and RCM output
401 (Box et al., 2013; Burgess et al., 2010; Fettweis et al., 2016; Noël et al., 2018). We analyze localized
402 differences between GPR derived accumulation and these RCMs in Section 3.3. There is an especially high
403 accumulation zone near Core 11 ($0.685 \text{ m w.e. } a^{-1}$), nearly double the accumulation at Core 10 ($0.453 \text{ m w.e. } a^{-1}$)
404 and Core 12 ($0.327 \text{ m w.e. } a^{-1}$), respectively situated only 43 km northwest and 73 km southwest of Core
405 11. In the GPR data, the number of traceable IRHs is highest towards the interior of the ice sheet and lowest
406 in warmer areas towards the coast and in the south, where refrozen percolated melt water from enhanced
407 surface melt attenuates the radar signal and reduces the number of observable IRHs (Brown et al., 2011;
408 Figure 3).

409 **3.2. Validation with past measurements**

410 We validate our accumulation record with published core records from the PARCA campaign and
411 accumulation data from the NASA IceBridge program. The locations of GreenTrACS Core sites 2, 5, 9, 10,
412 11, 14, 15, and 16 were chosen to reoccupy PARCA core locations 6745, 6945, 7147, 7247, 7249, NASA-
413 U, 7347, and 7345, respectively. These GreenTrACS cores overlap with the accumulation history of each
414 PARCA core and extend the record from 1997/1998 to 2016/2017. Accumulation rates derived from
415 GreenTrACS firn cores are within error of those determined from corresponding PARCA cores during the
416 period of overlap. Figure 5 compares the accumulation records from PARCA sites 6745, 6945, 7345, and
417 NASA-U to their corresponding GreenTrACS cores, demonstrating that each pair of cores has similar long-
418 term mean accumulation and nearly identical decadal variability. Thus, we have confidence in firn core



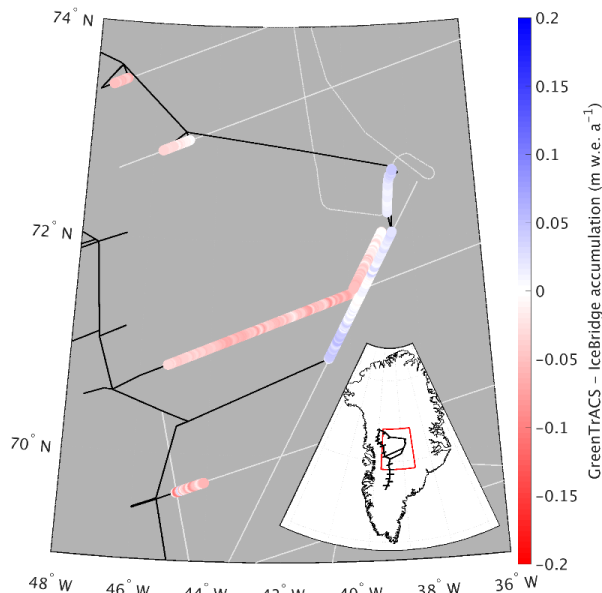
419 derived accumulation rates that are used in subsequent GPR calculations of accumulation rates throughout
420 the GreenTrACS traverse.
421



422
423 **Figure 5.** Accumulation from GPR and collected firn cores (this study) compared with cores from the PARCA Campaign. Thin lines
424 represent annual PARCA (blue) and GreenTrACS (black) firn core accumulation, while thick lines are 5-year averages over
425 corresponding GPR epochs. Error bars represent one standard deviation over each epoch. GPR and PARCA accumulation averages
426 and decadal trends are statistically indistinguishable.

427
428 Average (1966 – 2016) GPR accumulation is statistically indistinguishable with average (1962 – 2014)
429 IceBridge Accumulation Radar measurements analyzed by Lewis et al. (2017), with an RMS difference of
430 $0.0387 \pm 0.0327 \text{ m w.e. } \text{a}^{-1}$ along a total of 562.5 km of overlap (Figure 6). The disagreement is largest at
431 lower elevations, where Herron and Langway (1980) density profiles used in Lewis et al. (2017) differ the
432 most from GreenTrACS firn core density profiles in the upper 30 m of firn, demonstrating the importance of
433 field observations for calibration and validation. The close agreement at higher elevations is illustrated in
434 Figure 7a, where our GreenTrACS accumulation measurements are statistically indistinguishable from the
435 IceBridge radar-derived accumulation (Lewis et al., 2017) along the 285 km A – A' transect on Figure 1.
436 Notice that the uncertainty in GreenTrACS accumulation progressively decreases higher in the percolation
437 zone and into the dry snow zone (towards the right in Figure 7) along this transect as density becomes less
438 heterogeneous from fewer melt layers (Graeter et al., 2018) and IRHs become easier to trace.

439
440



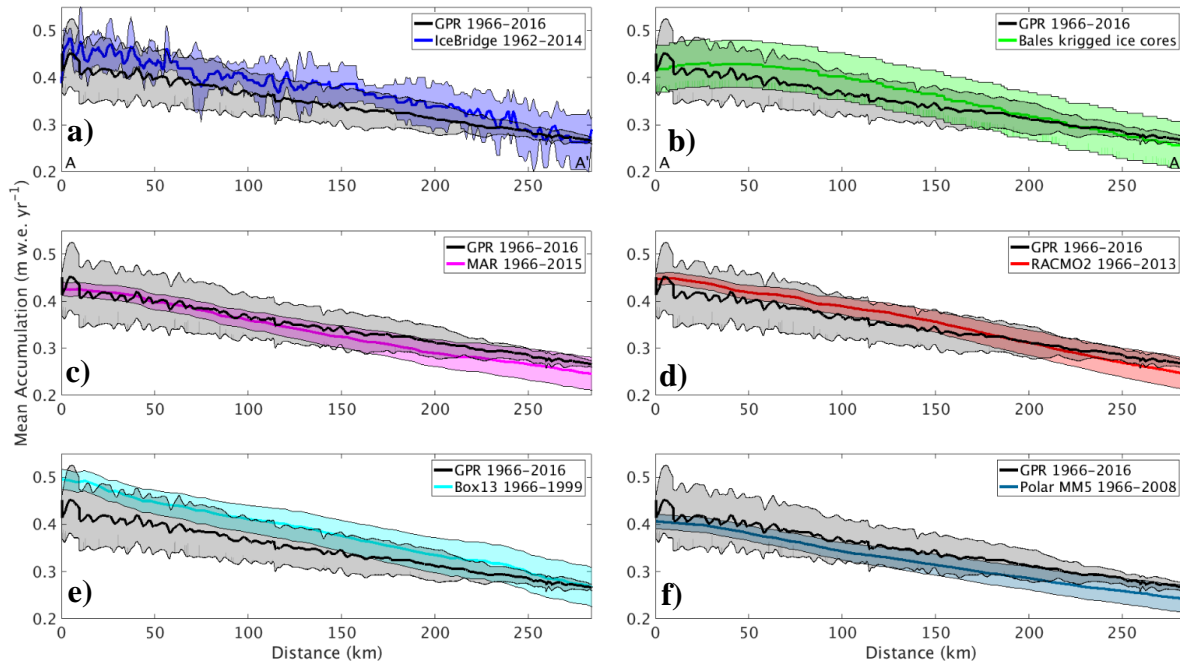
441

442 **Figure 6.** Difference between averaged (1966 – 2016) GreenTrACS accumulation and average (1962 – 2014) IceBridge Accumulation
443 Radar rates from Lewis et al. (2017) across all 562.5 km of overlap. Spatially overlapping section of 2016 and 2017 traverses displayed
444 as adjacent tracks. Also showing extent of GreenTrACS traverse (black) and IceBridge accumulation radar (grey). Inset shows map
445 location with respect to GreenTrACS traverse (black).

446

447 3.3. Comparison to modelled accumulation

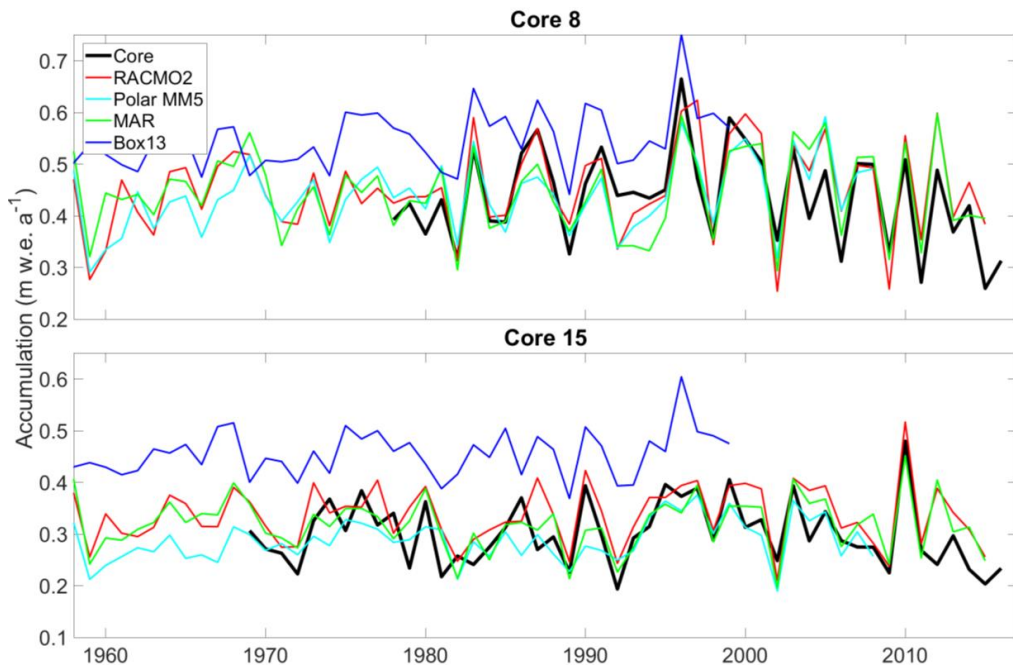
448 We assess differences between RCM accumulation output and GreenTrACS accumulation record at each firn
449 core site, two of which are shown in Figure 8. In general, year-to-year correlations between GreenTrACS
450 firn core accumulation records and RCM output for the corresponding grid cell are strong, positive, and
451 statistically significant (Table 2). On average, GreenTrACS firn cores' correlation coefficient with MAR
452 output is 0.718, with PolarMM5 is 0.701, with Box13 is 0.607, and with RACMO2 is 0.763. Every correlation
453 is statistically significant at $p < 0.05$ except for Cores 7 and 11 with Box13. We do not report a correlation
454 coefficient for Core 11 and Box13 because they only share two common years. Temporal correlation
455 coefficients remain high even at locations with large magnitude differences between RCM output and firn
456 core accumulation. For example, the Box13 model overestimates accumulation at Core 15 by 0.15 ± 0.05 m
457 w.e. a^{-1} , on average, but the model output has a correlation coefficient of 0.48 with Core 15 (Table 2) and
458 matches years of high accumulation (e.g. 1987, 1990, and 1996) and low accumulation (e.g. 1981, 1989,
459 1992).



460

461 **Figure 7.** Average GreenTrACS GPR accumulation (black) compared with a) IceBridge accumulation radar,
 462 b) Bales09 kriged ice core map, c) MAR, d) RACMO2, e) Box13, and f) Polar MM5. GPR measurements are statistically
 463 indistinguishable from each of the other measurements along this 285 km transect in the dry snow zone (A – A' on Figure 1).

464



465

466 **Figure 8.** Accumulation record at GreenTrACS Core 8 and Core 15 (black) compared with RCM output from RACMO2 (red),
 467 Polar MM5 (cyan), MAR (green), and Box13 (blue). We find statistically significant Pearson correlation coefficients
 468 between GreenTrACS and RCM accumulation rates for these cores (see Table 2).



469

470 Table 2. Pearson correlation coefficients between accumulation rate time series from firn cores and co-located RCM output over their
471 common time period[#].

	Available data period	MAR	PolarMM5	Box13	RACMO2
Core1	1966 – 2016	0.70	0.66	0.56	0.73
Core2	1969 – 2016	0.75	0.77	0.62	0.79
Core3	1971 – 2016	0.72	0.69	0.63	0.74
Core4	1977 – 2016	0.79	0.74	0.72	0.72
Core5	1984 – 2016	0.81	0.80	0.60	0.79
Core6	1985 – 2016	0.76	0.76	0.65	0.83
Core7	1993 – 2016	0.81	0.82	0.61	0.73
Core8	1978 – 2017	0.78	0.77	0.69	0.81
Core9	1984 – 2017	0.68	0.75	0.74	0.79
Core10	1984 – 2017	0.88	0.80	0.80	0.80
Core11	1997 – 2017	0.75	0.59	N/A	0.75
Core12	1962 – 2017	0.6	0.54	0.53	0.64
Core13	1955 – 2017	0.51	0.62	0.37	0.76
Core14	1974 – 2017	0.70	0.62	0.46	0.74
Core15	1969 – 2017	0.68	0.63	0.48	0.75
Core16	1979 – 2017	0.79	0.77	0.66	0.88

472 [#]Statistically significant correlations ($p < 0.05$) are bold

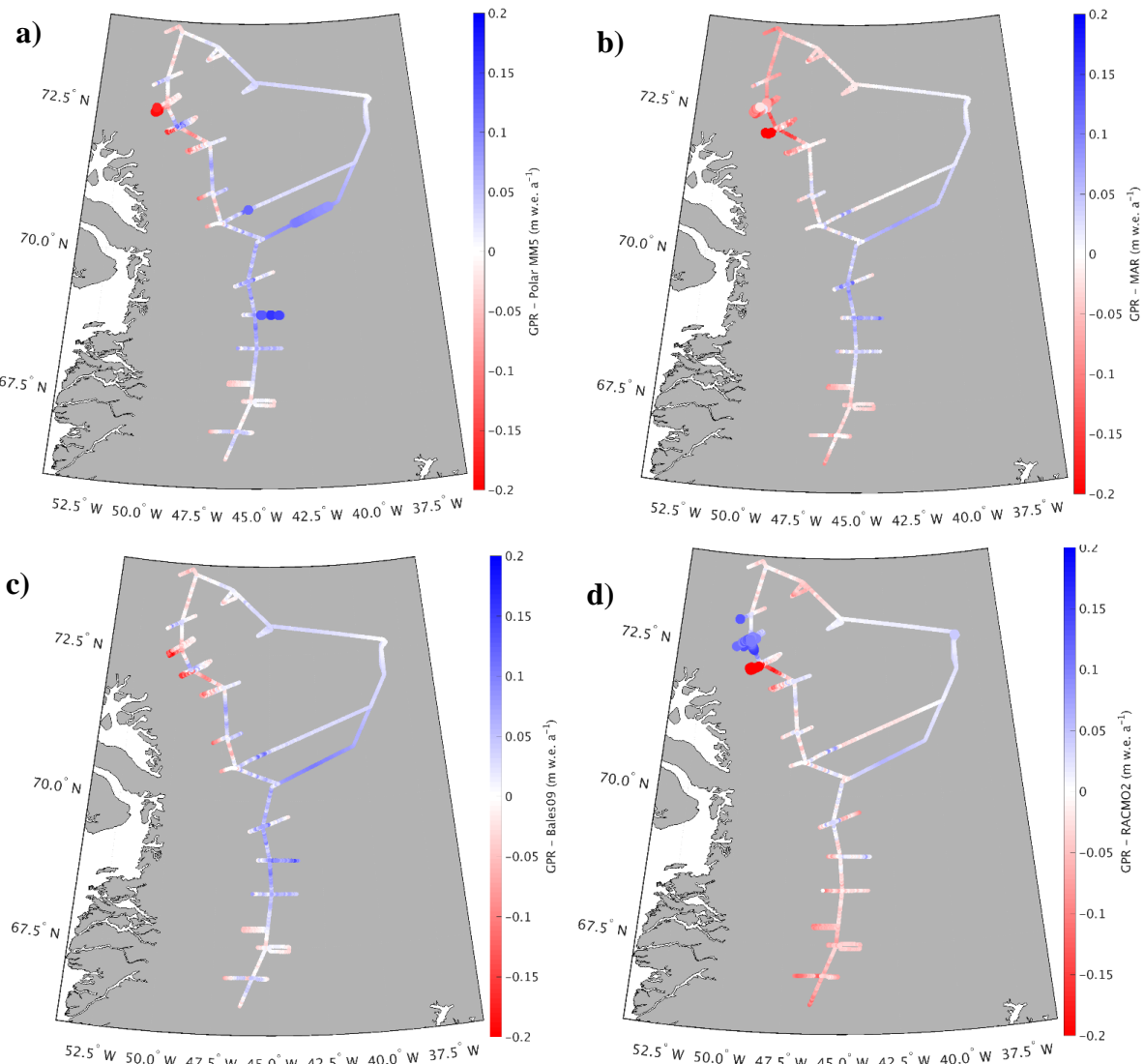
473

474 We also assess spatial differences between GreenTrACS accumulation and mean RCM accumulation
475 averaged over several decades. Figure 9 shows that differences between GreenTrACS accumulation and
476 RCM output increase in magnitude, become more spatially heterogeneous, and vary by model at lower
477 elevations of the ice sheet where topographic variations are larger and surface melt increases. Averaged over
478 all 4436 km of the traverse, the RMS difference between each model and GreenTrACS accumulation is 0.068
479 ± 0.065 (MAR), 0.0562 ± 0.0548 (RACMO2), 0.0822 ± 0.0702 (Box13), 0.048 ± 0.045 (Polar MM5), and
480 0.0475 ± 0.0445 m w.e. a^{-1} (Bales09). We find that RCM differences from GreenTrACS accumulation are
481 small in the dry snow zone (Figure 9). For example, Figure 7 shows that average GreenTrACS accumulation
482 measurements from 1966 – 2016 along the A – A' transect in Figure 1 are statistically indistinguishable from
483 those derived from the Bales09 krigged ice core map (Figure 7b), MAR (1966 – 2015; Figure 7c), RACMO2
484 (1966 – 2013; Figure 7d), Box13 (1966 – 1999; Figure 7e), and Polar MM5 (1966 – 2008; Figure 7f).

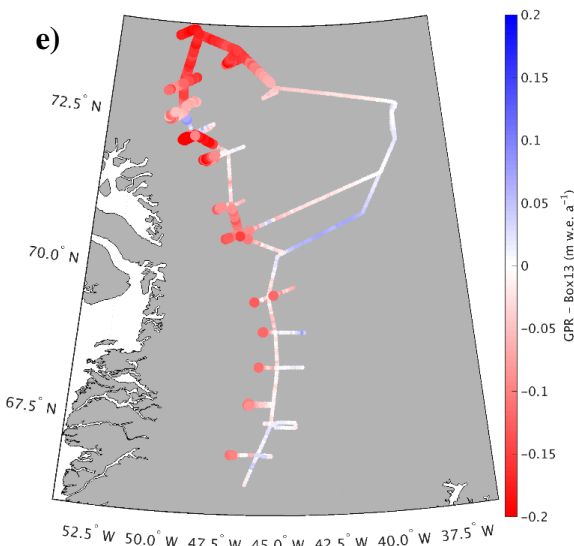
485

486 However, the high spatial resolution of our dataset shows significant accumulation variability not captured
487 in model output (Figure 9). For example, Polar MM5 and MAR both underestimate accumulation between
488 Core 4 and Summit, while overestimating accumulation to the west of Cores 10 – 12. Likewise, RACMO2
489 overestimates accumulation between Raven/Dye-2 and Core 5 by 0.03 to 0.08 m w.e. a^{-1} and shows
490 statistically significant differences east of Cores 11 and 12. Bales09 accurately calculates accumulation along
491 most of the 2016 traverse, but overestimates accumulation west of Cores 11 and 12 by 0.135 ± 0.041 m w.e.

492 a⁻¹. Finally, Box13 overestimates accumulation along many of the western spurs and has statistically
 493 significant overestimations of 0.1 to 0.4 m w.e. a⁻¹ between Cores 10 and 16. Box13 overestimates 67.8% of
 494 the data in the Core 10 – 16 region by at least 0.1 m w.e. a⁻¹, and 6.6% of that data by at least 0.2 m w.e. a⁻¹.
 495
 496 Our study is almost entirely contained within drainage basin E from Vernon et al. (2013), who note that basin
 497 E is the only major Greenland drainage basin with no statistically significant differences in SMB between
 498 the four RCMs. However, differences of 0.1 to 0.4 m w.e. a⁻¹ exist when we look at a local (sub-drainage-
 499 basin) scale for each model. All four of the RCMs overestimate accumulation along the western spur of Core
 500 11 and they all underestimate accumulation along the eastern spur of Core 5 (Figure 9).
 501



504



505

506 **Figure 9.** Differences between GreenTrACS accumulation and a) Polar MM5, b) MAR, c) Bales09, d) RACMO2, and e) Box13
507 accumulation averaged over the corresponding time periods. Large dots show statistically significant differences from GreenTrACS
508 accumulation.

509

510 In summary, the RCMs do an excellent job of calculating accumulation averaged over this drainage basin,
511 with RMS values between 0.048 and 0.0822 m w.e. a^{-1} , but there are larger differences of 0.1 to 0.4 m w.e.
512 a^{-1} between model and GPR accumulation on local scales. Differences between GreenTrACS and RCM
513 accumulation are largest in areas concurrent with the fewest, shortest, and/or most outdated *in situ*
514 measurements. For example, the GPR vs. model differences near Cores 11, 12, and 13 are relatively large for
515 all RCMs, despite Core 11 being co-located with PARCA 7249. However, the PARCA cores were collected
516 over 20 years ago, and Core 11 only spanned 7 years because of the high accumulation rate at that site. This
517 highlights the importance of collecting updated field-based measurements to calibrate remotely sensed data
518 and RCM output.

519

520 **3.4. Accumulation temporal trends**

521 In most locations, there are no statistically significant trends in the GreenTrACS accumulation record from
522 1966 through the mid-1990s. However, a changepoint analysis (Lavielle, 2005) reveals that accumulation in
523 the Western GrIS percolation zone changed significantly after the 1995 – 1996 accumulation year. Since
524 1996, our record indicates a statistically significant average accumulation decrease of 0.009 ± 0.005 m w.e
525 a^2 , or $2.4 \pm 1.5\% a^{-1}$, from 1996 to 2017. Although we observe fewer statistically significant accumulation



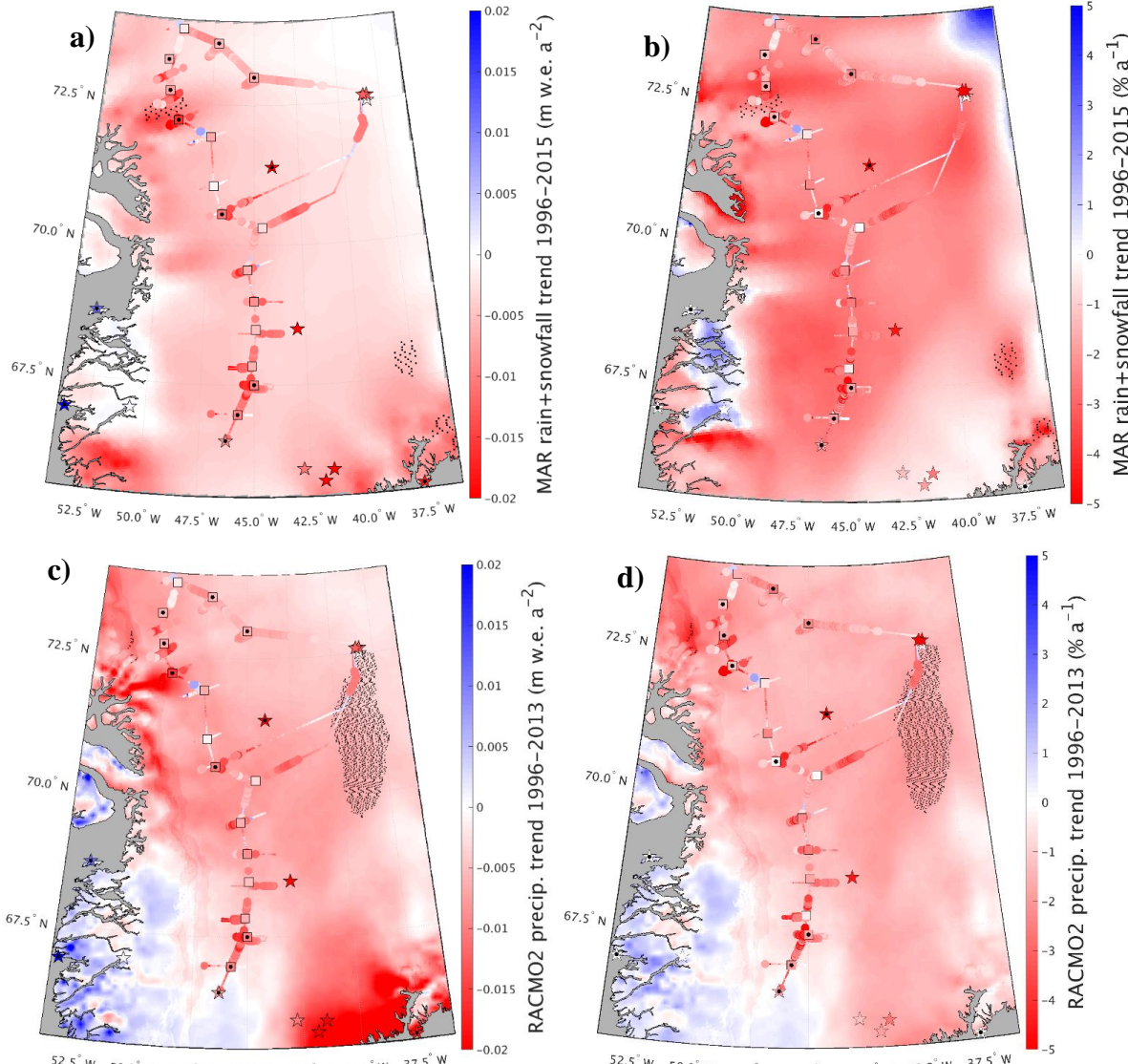
526 trends when we expand this analysis to include the entire temporal duration for each firn core, the sign of the
527 trend at each core site does not change.

528

529 In Figure 10, we compare the negative accumulation trend in the GreenTrACS record (1996 – 2016) to best-
530 fit linear trends in total precipitation (rain + snowfall) across the ice sheet in MAR and RACMO2 simulations
531 over the 1996 – 2015 and 1996 – 2013 periods, respectively. Also shown in Figure 10 are 1996 – 2016
532 accumulation trends for all 16 GreenTrACS firn cores (squares), accumulation trends from ACT10A (1996
533 – 2010), ACT10B (1996 – 2010), ACT10C (1996 – 2010), D4 (1991 – 2002), D5 (1991 – 2002), Katie (1991
534 – 2002), Sandy (1991 – 2002), and Summit 2010 (1991 – 2010) ice/firn cores (stars on ice sheet), and
535 precipitation trends from coastal weather stations (Mernild et al., 2014; stars on coast). Statistically
536 significant trends ($p < 0.05$) in core data are indicated by black dots, while statistically significant trends in
537 the MAR and RACMO2 output are stippled in black.

538

539 We find strong agreement between the accumulation decrease in the GreenTrACS record and widespread
540 precipitation decreases in the RCMs over the study area (Figure 10). On average, the RCMs have a more
541 negative precipitation trend than the GreenTrACS record by 0.003 ± 0.005 for MAR and 0.0016 ± 0.0051 m
542 w.e. a^{-2} for RACMO2. Vernon et al. (2013) show a melt-driven decrease in SMB across this drainage basin
543 of 31.1% (ECMWFd), 61.6% (RACMO2), 76.5% (MAR), and 33.5% (Polar MM5) for the 1996 – 2008
544 period. The negative precipitation trends of $2.4 \pm 1.5\% a^{-1}$ (Figure 10d) indicate a total of 2539.4 fewer Gt
545 of precipitation and a total of 5159.1 additional Gt of melt (not shown) over 1996 – 2013 across the GrIS.
546 Thus, our analysis suggests that a significant decline in snow accumulation contributes to declining SMB
547 throughout the Western GrIS over recent decades, in addition to increasing surface melt from rising
548 temperatures (van den Broeke et al., 2009, 2016).



549

550

551 **Figure 10.** Best fit linear trends for each grid cell showing magnitude (left) and percent (right) changes in total precipitation for a) and
 552 b) MAR (1996 – 2015) and c) and d) RACMO2 (1996 – 2013). Statistically significant RCM grid cell trends are stippled black.
 553 Also shown are accumulation trends for GreenTrACS firn cores (squares), ACT10A, ACT10B, ACT10C, D4, D5, Katie, Sandy, Summit 2010,
 554 and Raven/Dye-2 cores (stars on ice sheet) and precipitation trends from Mernild et al (2014; stars on coast) with statistically significant
 555 trends indicated by black dots.

556

557 3.5. Effects of melt on accumulation trends

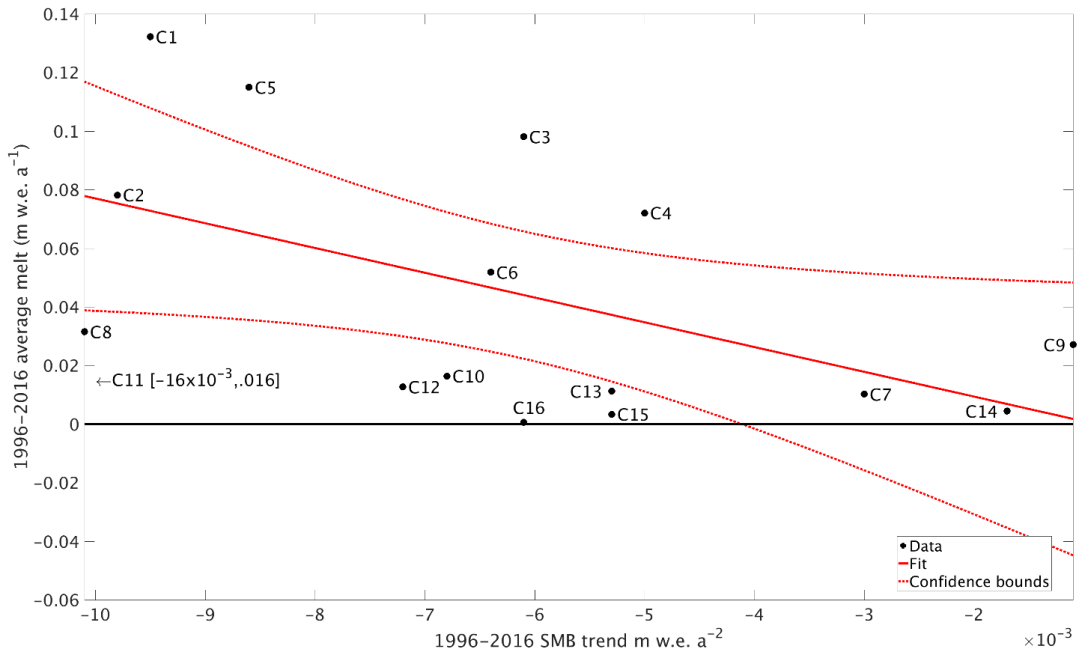
558 Increased melt throughout the 1996 – 2016 period is a confounding variable when analyzing trends in
 559 accumulation. With increased melt over the past several decades in this region, meltwater percolates down
 560 through several years of firn (Benson, 1962; Graeter et al., 2018; Harper et al., 2012; Wong et al., 2013).



561 This movement of mass into lower years can artificially increase the mass balance at depth and lower the
562 mass balance during the most recent years, which have not experienced as much meltwater percolation from
563 more recent annual layers. Therefore, it is necessary to evaluate the degree to which the recent accumulation
564 decrease in the GreenTrACS record is biased by the recent increase in surface melt and percolation.
565

566 Figure 11 compares the 1996 – 2016 mass balance trends with 1996 – 2016 average melt for each of the
567 sixteen GreenTrACS firn cores. If we exclude Core 11 (which only dates back to 1997 and has a highly
568 negative SMB trend), the linear regression is statistically significant with $p = 0.04$ (Figure 11). Note that both
569 the measured Core 11 SMB trend and RCM trends at that location are so negative, with that small amount of
570 average melt, that the linear trend is no longer significant if that point is included in the calculations. On
571 average, we find larger negative accumulation trends (-7×10^{-3} to -10×10^{-3} m w.e. a^{-2}) at the lower latitude
572 cores that experience more melt, supporting the hypothesis that meltwater percolation and refreezing are
573 enhancing the negative accumulation trend.
574

575 However, several other lines of evidence support a negative accumulation trend in the study area since 1996.
576 First, we find statistically significant negative accumulation trends at Cores 10, 11, 12, 13, 15, and 16, each
577 of which experience <1.6 cm a^{-1} of meltwater percolation on average (Figure 11). Additionally, we have
578 confidence that GreenTrACS accumulation trends reported here are not artifacts of meltwater percolation
579 because both MAR and RACMO2 have similar trends in precipitation (Figure 10). Finally, we evaluate the
580 maximum effect meltwater percolation could have on GreenTrACS accumulation trends over 1996 – 2016.
581 The largest melt layer from our sixteen ice cores occurred during 2003 – 2004 in Core 1 and contains 0.364
582 m of ice, equivalent to 0.333 m w.e. (Graeter et al., 2018). We add this percolation to nine years' of
583 accumulation using a sine wave (percolation magnitude 0, 0.5, 1, 0.5, 0, -0.5, -1, -0.5, 0), square wave (0, 0,
584 0, 1, 1, 1, 0, 0, 0), and triangle wave (0, 0.25, 0.5, 0.75, 1, 0.75, 0.5, 0.25, 0) weighted kernel, before re-
585 computing hypothetical accumulation trends over the same time period with additional meltwater
586 percolation. Regardless of the wave-type choice, re-calculated trends remain within a factor of two of the
587 original SMB trends and do not change sign with additional percolation.
588



589

590 **Figure 11.** Relationship between 1996 – 2016 SMB trend and 1996 – 2016 melt for each of the 16 GreenTrACS firn cores (black circles).
 591 Red line shows linear best fit, dotted line shows 95% confidence boundary.

592

3.6. Atmospheric circulation drivers of the recent accumulation decline

593

Our analysis indicates that snow accumulation has been declining in Western Greenland since 1996, despite significant warming and resulting increases in saturation vapor pressure from the Clausius-Clapeyron relationship. Instead, precipitation decreases over Western Greenland likely result from changes in atmospheric and/or oceanic circulation. Mernild et al. (2014) and Auger et al. (2017) found that the positive phase of the Atlantic Multidecadal Oscillation (AMO) is associated with a precipitation increase over interior and Southwestern Greenland based on ice core records and the Japanese Meteorological Agency 55 Year Reanalysis (JRA-55; Kobayashi et al., 2015), respectively. In direct contrast with these findings, the decline in Western Greenland accumulation documented in the GreenTrACS record began in the mid-1990s, contemporaneous with a switch to the AMO positive phase.

602

603

We hypothesize that the differences between our results and those of Auger et al. (2017) and Mernild et al. (2014) stem from different causes. Auger et al. (2017) validated the reanalysis data by demonstrating that JRA-55 precipitation at Nuuk, Greenland is significantly correlated with Nuuk station data from 1958 – 2013. Furthermore, coastal precipitation in Western Greenland is strongly and significantly ($p < 0.05$) correlated with precipitation over the interior Western GrIS in the JRA-55 dataset (not shown). However, Mernild et al. (2014) found that coastal Greenland precipitation is anti-correlated with ice core accumulation records from



the interior GrIS from 1900 to 2000. This suggests that JRA-55 precipitation data, which is not constrained by ice core accumulation records, should be interpreted with caution over the interior GrIS. Mernild et al. (2014) concluded that positive AMO conditions favor higher precipitation over the interior GrIS based on the previous positive AMO phase (1920s to mid-1960s), contrasting with lower accumulation during the negative AMO phases (mid-1960s to mid-1990s and prior to the 1920s). However, Mernild et al. (2014) state that the ice core composite record in their analysis may be biased from 1995 – 2000, and they do not analyze precipitation trends after 2000. Thus, the decline in Western GrIS accumulation documented in the GreenTrACS cores during the latest positive AMO phase from 1996 to 2017 was not captured in the Mernild et al. (2014) analysis. Our results suggest that factors other than the AMO are behind the decline in Western GrIS accumulation since 1996.

619

We find that the decrease in accumulation over the Western GrIS is associated with a significant decrease in the number of storm-days since 1996. The GreenTrACS region experienced an average of 115.8 ± 15.3 storm-days per year over 1958 – 1996 and 96.2 ± 27.3 storm-days per year over 1996 – 2016. A two sample t-test indicates that this 17% decline in storm-days is statistically significant ($p < 0.001$). The largest decrease in storm-days (25%) over the GreenTrACS region occurred during summer, with 56.4 ± 6.1 storm-days per summer from 1958 – 1996 and 42.3 ± 17.4 storm-days per summer from 1996 – 2016 ($p < 0.0001$; Figure 12b). We also find an increase in the number of storm-days in the Northwestern GrIS near Thule (not shown).

627

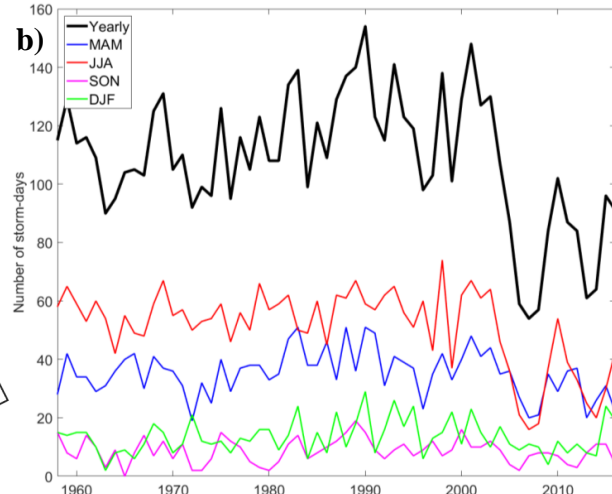
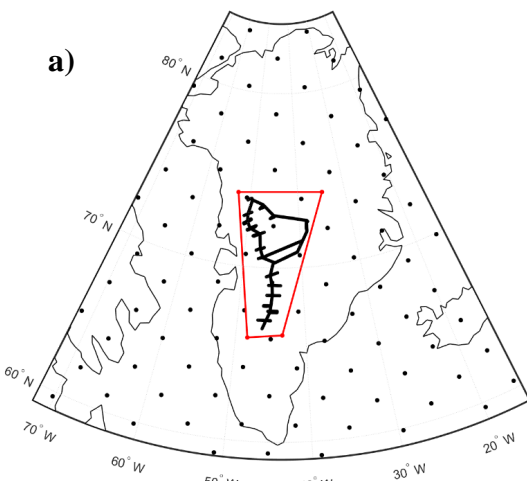
The decline in summer storm-days indicates a relationship with well-documented stronger summer blocking over Greenland over the past two decades (Hanna et al., 2013; McLeod and Mote, 2016), with a positive Greenland Blocking Index during 17 out of 21 summers between 1996 – 2016 (Hanna et al., 2016). The June – August GBI had a statistically significant positive trend of 1.87 (unitless; normalized to 1951 – 2000) from 1991 – 2015 (Hanna et al., 2016). The summertime 500 mbar geopotential height increased 50 – 70 m over the 1996 – 2016 period compared with the 1979 – 1996 baseline (Figure 12c), indicating stronger blocking that we suggest likely reduced precipitation over the central GrIS by deflecting storms poleward from the Greenland interior. This is consistent with an observed $0.9 \pm 0.3\%$ a^{-1} decrease in JJA cloud cover over Greenland from 1995-2009, with the largest decreases in the GreenTrACS region (Hofer et al., 2017). Furthermore, we find a strong negative correlation between ERA-Interim 1979 – 2015 June – August (JJA) GBI and JJA precipitation in both MAR (Figure 12d) and RACMO2 (not shown) across the central and southern GrIS. These results suggest that the blocking-induced accumulation decline observed in the GreenTrACS region is representative of a broader pattern over the GrIS, with the exception of Northwest Greenland where poleward blocking has increased storm-days (not shown) and accumulation (Figure 12d).

642

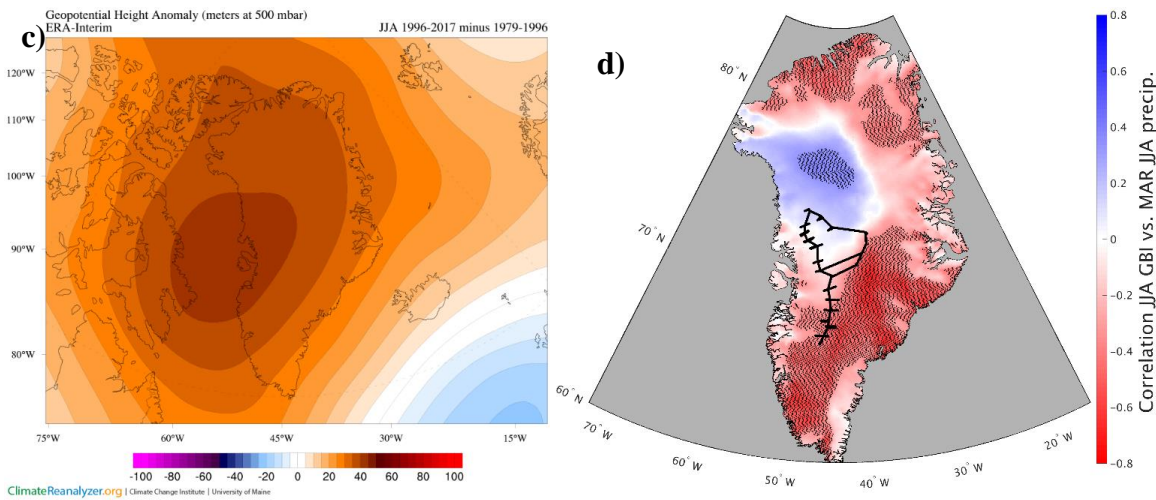


643

644 The effect of summertime Greenland blocking has been discussed primarily in the context of increasing
645 surface melt (Hanna et al.. 2013; Ballinger et al., 2017; Hanna et al., 2018; Hofer et al., 2017), while the
646 effect of blocking on precipitation has received less attention (Hanna et al., 2013; McLeod and Mote, 2016).
647 Our results highlight that stronger summer blocking reduces GrIS SMB through both an increase in surface
648 melting and a decrease in accumulation. Stronger summer blocking has been tied to an observed increase in
649 surface melt since 1996 across the Western GrIS percolation zone (Graeter et al., 2018), and to the July 2012
650 melt event, during which 98.6% of the GrIS experienced melt (Nghiem et al., 2012). We show here with *in*
651 *situ* data that snow accumulation has declined in this same region as strong blocking has decreased the
652 number of summer storm-days. Presently, none of the GBI outputs from the Coupled Model Intercomparison
653 Project 5 (CMIP5) suite of global climate models accurately capture the recent summer GBI increase (Hanna
654 et al., 2018). Improved predictions of summertime Greenland blocking under future anthropogenic forcing
655 scenarios are therefore critical for accurately predicting Greenland SMB and its contribution to sea level rise.
656



657



658

659

660 **Figure 12.** a) (Serreze, 2009) gridded storm track dataset showing location of GreenTrACS
 661 traverse and inquiry box. b) Total number
 662 of storm-days within inquiry box for annual and seasonal periods. Horizontal black lines show a
 663 decrease in 1958 – 1996 to 1996 – 2016
 664 average number of storm-days within this region. c) 500 mbar geopotential height change over
 665 Greenland showing 1996 – 2016 minus
 1979 – 1996 for the summer season. Image obtained using Climate Reanalyzer (<http://cci-reanalyzer.org>), Climate Change Institute,
 University of Maine, United States. d) Correlation between June – August Greenland Blocking Index and MAR June – August
 precipitation. Statistically significant RCM grid cell correlations are stippled black. GreenTrACS traverse is shown in black.

666 4. Conclusions

667 We have developed a new dataset of accumulation rates over the western interior of the Greenland ice sheet
 668 spanning the past 20 – 60 years, based on sixteen 22 – 32 m long firn cores and 4436 km of *in situ* GPR
 669 accumulation data. This accumulation record is internally consistent across the dataset and is validated by
 670 previous *in situ* field measurements and other radar-derived accumulation measurements (e.g Lewis et al.,
 671 2017).

672

673 Overall, the Polar MM5, MAR, Box13, and RACMO2 Regional Climate Models accurately capture large
 674 spatial patterns in accumulation over the GrIS, but show statistically significant differences from GPR
 675 accumulation on a regional basis. The average RMS difference between each model and GreenTrACS
 676 accumulation is 0.068 ± 0.065 (MAR), 0.048 ± 0.045 (Polar MM5), 0.0822 ± 0.0702 (Box13), $0.0562 \pm$
 677 0.0548 (RACMO2), and 0.0475 ± 0.0445 m w.e. a^{-1} (Bales09). These differences are on the same order as
 678 the uncertainties in the GreenTrACS and RCM accumulation estimates. While these average differences are
 679 small, we find differences of 0.1 to 0.4 m w.e. a^{-1} when we investigate at a local scale for each model.

680

681 While global climate models predict a 21st-century increase in precipitation over the GrIS (e.g. Bintanja and
 682 Seltten, 2014), we observe a decrease in precipitation across the Western GrIS from 1996 – 2016 using records



683 from firn cores, GPR, and published RCMs. We believe this study is the first to identify widespread negative
684 GrIS precipitation trends during this period of enhanced surface melt, evident in these RCMs and our field
685 observations (Graeter et al., 2018).

686

687 We attribute the decrease in accumulation over the Western GrIS between 1996 and 2016 to more persistently
688 positive Greenland blocking in the summer. We find a statistically significant 25% reduction in the number
689 of summer storms that precipitate over the GreenTrACS region since 1996. While warming temperatures
690 from anthropogenic forcing and enhanced summer blocking have increased melt across the western
691 percolation zone, here we show that summer blocking has also contributed to declining precipitation over the
692 past two decades. This has led to a strongly negative SMB trend on both the input and output sides of the
693 SMB equation that may not be accurately captured in global climate models that are currently unable to
694 reproduce the recent increase in blocking. This highlights the importance of improving GCM projections of
695 future summer blocking to accurately forecast Greenland precipitation and melt rates under stronger
696 greenhouse gas forcing.

697 **5. Works cited**

- 698 Auger, J. D., Birkel, S. D., Maasch, K. A., Mayewski, P. A. and Schuenemann, K. C.: Examination of
699 precipitation variability in southern Greenland, *J. Geophys. Res.*, 122(12), 6202–6216,
700 doi:10.1002/2016JD026377, 2017.
- 701 Bales, R. C., Guo, Q., Shen, D., McConnell, J. R., Du, G., Burkhardt, J. F., Spikes, V. B., Hanna, E. and
702 Cappelen, J.: Annual accumulation for Greenland updated using ice core data developed during 2000-2006
703 and analysis of daily coastal meteorological data, *J. Geophys. Res. Atmos.*, 114(6), D06116,
704 doi:10.1029/2008JD011208, 2009.
- 705 Ballinger, T. J., Hanna, E., Hall, R. J., Cropper, T. E., Miller, J., Ribergaard, M. H., Overland, J. E. and
706 Høyer, J. L.: Anomalous blocking over Greenland preceded the 2013 extreme early melt of local sea ice,
707 *Ann. Glaciol.*, 2013(March 2013), 1–10, doi:10.1017/aog.2017.30, 2017.
- 708 Banta, J. R. and McConnell, J. R.: Annual accumulation over recent centuries at four sites in central
709 Greenland, *J. Geophys. Res. Atmos.*, 112(10), 1–9, doi:10.1029/2006JD007887, 2007.
- 710 Benson, C. S.: Stratigraphic studies in the snow and firn of the Greenland Ice Sheet, *Folia Geogr. Danica*, 9,
711 13–37, 1962.
- 712 Bevington, P. R. and Robinson, D. K.: Data Reduction and Error Analysis for the Physical Sciences, 2nd
713 Editio., McGraw-Hill., 1992.
- 714 Bintanja, R. and Selten, F. M.: Future increases in Arctic precipitation linked to local evaporation and sea-
715 ice retreat, *Nature*, 509(7501), 479–482, doi:10.1038/nature13259, 2014.
- 716 Box, J. E.: Survey of greenland instrumental temperature records: 1873-2001, *Int. J. Climatol.*, 22(15), 1829–
717 1847, doi:10.1002/joc.852, 2002.
- 718 Box, J. E., Bromwich, D. H., Veenhuis, B. a., Bai, L. S., Stroeve, J. C., Rogers, J. C., Steffen, K., Haran, T.
719 and Wang, S. H.: Greenland Ice Sheet Surface Mass Balance Variability (1988 – 2004) from Calibrated



- 720 Polar MM5 Output *, J. Clim., 19(12), 2783–2801, doi:doi.org/10.1175/JCLI3738.1, 2006.
- 721 Box, J. E., Cressie, N., Bromwich, D. H., Jung, J. H., van den Broeke, M. R., van Angelen, J. H., Forster, R.
722 R., Miège, C., Mosley-Thompson, E., Vinther, B. and McConnell, J. R.: Greenland ice sheet mass balance
723 reconstruction. Part I: Net snow accumulation (1600–2009), J. Clim., 26(11), 3919–3934, doi:[10.1175/JCLI-D-12-00373.1](https://doi.org/10.1175/JCLI-D-12-00373.1), 2013.
- 724 van den Broeke, M. R., Bamber, J. L., Ettema, J., Rignot, E. J., Schrama, E., van de Berg, W. J., van
725 Meijgaard, E., Velicogna, I. and Wouters, B.: Partitioning recent Greenland mass loss., Science, 326(5955),
726 984–6, doi:[10.1126/science.1178176](https://doi.org/10.1126/science.1178176), 2009.
- 727 van den Broeke, M. R., Enderlin, E. M., Howat, I. M., Kuipers Munneke, P., Noël, B., van de Berg, W. J., van
728 Meijgaard, E. and Wouters, B.: On the recent contribution of the Greenland ice sheet to sea level change,
729 Cryosph. Discuss., 1–26, doi:[10.5194/tc-2016-123](https://doi.org/10.5194/tc-2016-123), 2016.
- 730 Brown, J., Harper, J., Pfeffer, W. T., Humphrey, N. and Bradford, J.: High-resolution study of layering within
731 the percolation and soaked facies of the Greenland ice sheet, Ann. Glaciol., 52(59), 35–42,
732 doi:[10.3189/172756411799096286](https://doi.org/10.3189/172756411799096286), 2011.
- 733 Buchardt, S. L., Clausen, H. B., Vinther, B. M. and Dahl-Jensen, D.: Investigating the past and recent $\delta^{18}\text{O}$ -
734 accumulation relationship seen in Greenland ice cores, Clim. Past, 8(6), 2053–2059, doi:[10.5194/cp-8-2053-2012](https://doi.org/10.5194/cp-8-2053-2012), 2012.
- 735 Burgess, E. W., Forster, R. R., Box, J. E., Mosley-Thompson, E., Bromwich, D. H., Bales, R. C. and Smith,
736 L. C.: A spatially calibrated model of annual accumulation rate on the Greenland Ice Sheet (1958–2007), J.
737 Geophys. Res. Earth Surf., 115(2), 1–14, doi:[10.1029/2009JF001293](https://doi.org/10.1029/2009JF001293), 2010.
- 738 Enderlin, E. M., Howat, I. M., Jeong, S., Noh, M. J., Van Angelen, J. H. and Van Den Broeke, M. R.: An
739 improved mass budget for the Greenland ice sheet, Geophys. Res. Lett., 41(3), 866–872,
740 doi:[10.1002/2013GL059010](https://doi.org/10.1002/2013GL059010), 2014.
- 741 Ettema, J., van den Broeke, M. R., van Meijgaard, E., van de Berg, W. J., Bamber, J. L., Box, J. E. and Bales,
742 R. C.: Higher surface mass balance of the Greenland ice sheet revealed by high-resolution climate modeling,
743 Geophys. Res. Lett., 36(12), L12501, doi:[10.1029/2009GL038110](https://doi.org/10.1029/2009GL038110), 2009.
- 744 Fettweis, X., Box, J. E., Agosta, C., Amory, C., Kittel, C. and Gallée, H.: Reconstructions of the 1900–2015
745 Greenland ice sheet surface mass balance using the regional climate MAR model, Cryosph. Discuss.,
746 (November), 1–32, doi:[10.5194/tc-2016-268](https://doi.org/10.5194/tc-2016-268), 2016.
- 747 Gerlitz, K., Knoll, M., Cross, G., Luzitano, R. and Knight, R.: Processing Ground Penetrating Radar Data to
748 Improve Resolution of Near-Surface Targets, in Symposium on the Application of Geophysics to
749 Engineering and Environmental Problems 1993, pp. 561–574, Environment and Engineering Geophysical
750 Society., 1993.
- 751 Graeter, K. A., Osterberg, E. C., Ferris, D., Hawley, R. L., Marshall, H. P. and Lewis, G.: Ice Core Records
752 of West Greenland Surface Melt and Climate Forcing, Geophys. Res. Lett., doi:[10.1002/2017GL076641](https://doi.org/10.1002/2017GL076641),
753 2018.
- 754 Hall, D. K., Box, J. E., Casey, K. A., Hook, S. J., Shuman, C. A. and Steffen, K.: Comparison of satellite-
755 derived and in-situ observations of ice and snow surface temperatures over Greenland, Remote Sens.
756 Environ., 112(10), 3739–3749, doi:[10.1016/j.rse.2008.05.007](https://doi.org/10.1016/j.rse.2008.05.007), 2008.
- 757 Hall, D. K., Comiso, J. C., DiGirolamo, N. E., Shuman, C. A., Key, J. R. and Koenig, L. S.: A satellite-
758 derived climate-quality data record of the clear-sky surface temperature of the Greenland ice sheet, J. Clim.,
759 25(14), 4785–4798, 2012.
- 760 Hall, D. K., Comiso, J. C., DiGirolamo, N. E., Shuman, C. A., Box, J. E. and Koenig, L. S.: Variability in
761 the surface temperature and melt extent of the Greenland ice sheet from MODIS, Geophys. Res. Lett., 40(10),
762 29



- 764 2114–2120, doi:10.1002/grl.50240, 2013.
- 765 Hanna, E., Mernild, S. H., Cappelen, J. and Steffen, K.: Recent warming in Greenland in a long-term
766 instrumental (1881–2012) climatic context: I. Evaluation of surface air temperature records, Environ. Res.
767 Lett., 7(4), 045404, doi:10.1088/1748-9326/7/4/045404, 2012.
- 768 Hanna, E., Jones, J. M., Cappelen, J., Mernild, S. H., Wood, L., Steffen, K. and Huybrechts, P.: The influence
769 of North Atlantic atmospheric and oceanic forcing effects on 1900–2010 Greenland summer climate and ice
770 melt/runoff, Int. J. Climatol., 33(4), 862–880, doi:10.1002/joc.3475, 2013.
- 771 Hanna, E., Cropper, T. E., Hall, R. J. and Cappelen, J.: Greenland Blocking Index 1851–2015: a regional
772 climate change signal, Int. J. Climatol., 36(15), 4847–4861, doi:10.1002/joc.4673, 2016.
- 773 Hanna, E., Fettweis, X. and Hall, R. J.: Recent changes in summer Greenland blocking captured by none of
774 the CMIP5 models, Cryosph. Discuss., 1–8, doi:10.5194/tc-2018-91, 2018.
- 775 Harper, J., Humphrey, N., Pfeffer, W. T., Brown, J. and Fettweis, X.: Greenland ice-sheet contribution to
776 sea-level rise buffered by meltwater storage in firn, Nature, 491(7423), 240–243, doi:10.1038/nature11566,
777 2012.
- 778 Hawley, R. L., Courville, Z. R., Kehrl, L. M., Lutz, E. R., Osterberg, E. C., Overly, T. B. and Wong, G. J.:
779 Recent accumulation variability in northwest Greenland from ground-penetrating radar and shallow cores
780 along the Greenland Inland Traverse, J. Glaciol., 60(220), 375–382, doi:10.3189/2014JoG13J141, 2014.
- 781 Herron, M. M. and Langway, C. C.: Firn densification: an empirical model., J. Glaciol., 25(93), 373–385,
782 doi:10.3198/1980JoG25-93-373-385, 1980.
- 783 Hofer, S., Bamber, J., Tedstone, A. and Fettweis, X.: Decreasing clouds drive mass loss on the Greenland
784 Ice Sheet, EGU Gen. Assem. Conf. Abstr., 19(6), 5086, 2017.
- 785 Karlöf, L., Isaksson, E., Winther, J. G., Gundestrup, N. S., Meijer, H. A. J., Mulvaney, R., Pourchet, M.,
786 Hofstede, C., Lappegard, G., Petterson, R., van den Broeke, M. R. and Van De Wal, R. S. W.: Accumulation
787 variability over a small area in east Dronning Maud Land, Antarctic, as determined from shallow firn cores
788 and snow pits: Some implications for ice-core records, J. Glaciol., 51(174), 343–352,
789 doi:10.3189/172756505781829232, 2005.
- 790 Kobayashi, S., Ota, Y., Harada, Y., Ebita, A., Moriya, M., Onoda, H., Onogi, K., Kamahori, H., Kobayashi,
791 C., Endo, H., Miyaoka, K. and Takahashi, K.: The JRA-55 Reanalysis: General Specifications and Basic
792 Characteristics, J. Meteorol. Soc. Japan. Ser. II, 93(1), 5–48, doi:10.2151/jmsj.2015-001, 2015.
- 793 Kovacs, A., Gow, A. J. and Morey, R. M.: The in-situ dielectric constant of polar firn revisited, Cold Reg.
794 Sci. Technol., 23(3), 245–256, doi:10.1016/0165-232X(94)00016-Q, 1995.
- 795 Lavielle, M.: Using penalized contrasts for the change-point problem, Signal Processing, 85(8), 1501–1510,
796 doi:10.1016/j.sigpro.2005.01.012, 2005.
- 797 Lewis, G., Osterberg, E. C., Hawley, R. L., Whitmore, B., Marshall, H. P. and Box, J. E.: Regional Greenland
798 accumulation variability from Operation IceBridge airborne accumulation radar, Cryosph., 11(2), 773–788,
799 doi:10.5194/tc-11-773-2017, 2017.
- 800 McGrath, D., Colgan, W., Bayou, N., Muto, A. and Steffen, K.: Recent warming at Summit, Greenland:
801 Global context and implications, Geophys. Res. Lett., 40(10), 2091–2096, doi:10.1002/grl.50456, 2013.
- 802 McLeod, J. T. and Mote, T. L.: Linking interannual variability in extreme Greenland blocking episodes to
803 the recent increase in summer melting across the Greenland ice sheet, Int. J. Climatol., 36(3), 1484–1499,
804 doi:10.1002/joc.4440, 2016.
- 805 Medley, B., Joughin, I., Das, S. B., Steig, E. J., Conway, H., Gogineni, S. P., Criscitiello, a. S., McConnell,
806 J. R., Smith, B. E., van den Broeke, M. R., Lenaerts, J. T. M., Bromwich, D. H. and Nicolas, J. P.: Airborne-



- 807 radar and ice-core observations of annual snow accumulation over Thwaites Glacier, West Antarctica
808 confirm the spatiotemporal variability of global and regional atmospheric models, *Geophys. Res. Lett.*,
809 40(14), 3649–3654, doi:10.1002/grl.50706, 2013.
- 810 Mernild, S. H., Hanna, E., McConnell, J. R., Sigl, M., Beckerman, A. P., Yde, J. C., Cappelen, J., Malmros,
811 J. K. and Steffen, K.: Greenland precipitation trends in a long-term instrumental climate context (1890–2012):
812 Evaluation of coastal and ice core records, *Int. J. Climatol.*, doi:10.1002/joc.3986, 2014.
- 813 Meyer, C. R. and Hewitt, I. J.: A continuum model for meltwater flow through compacting snow, *Cryosphere*,
814 11(6), 2799–2813, doi:10.5194/tc-11-2799-2017, 2017.
- 815 Morlighem, M., Rignot, E. J., Mouginot, J., Seroussi, H. and Larour, E.: Deeply incised submarine glacial
816 valleys beneath the Greenland ice sheet, *Nat. Geosci.*, 7(6), 18–22, doi:10.1038/ngeo2167, 2014.
- 817 Morris, E. M. and Wingham, D. J.: Densification of polar snow: Measurements, modeling, and implications
818 for altimetry, *J. Geophys. Res. Earth Surf.*, 119(2), 349–365, doi:10.1002/2013JF002898, 2014.
- 819 Mosley-Thompson, E., McConnell, J. R., Bales, R. C., Li, Z., Lin, P.-N., Steffen, K., Thompson, L. G.,
820 Edwards, R. and Bathke, D.: Local to regional-scale variability of annual net accumulation on the Greenland
821 ice sheet from PARCA cores, *J. Geophys. Res.*, 106(D24), 33839, doi:10.1029/2001JD900067, 2001.
- 822 Mouginot, J., Rignot, E., Bjørk, A. A., van den Broeke, M., Millan, R., Morlighem, M., Noël, B., Scheuchl,
823 B. and Wood, M.: Forty-six years of Greenland Ice Sheet mass balance from 1972 to 2018, *Proc. Natl. Acad.
824 Sci.*, 201904242, doi:10.1073/pnas.1904242116, 2019.
- 825 Nghiem, S. V., Steffen, K., Neumann, G. and Huf, R.: Mapping of ice layer extent and snow accumulation
826 in the percolation zone of the Greenland ice sheet, *J. Geophys. Res. Earth Surf.*, 110(2), 1–13,
827 doi:10.1029/2004JF000234, 2005.
- 828 Nghiem, S. V., Hall, D. K., Mote, T. L., Tedesco, M., Albert, M. R., Keegan, K., Shuman, C. A., DiGirolamo,
829 N. E. and Neumann, G.: The extreme melt across the Greenland ice sheet in 2012, *Geophys. Res. Lett.*,
830 39(20), 6–11, doi:10.1029/2012GL053611, 2012.
- 831 Noël, B., van de Berg, W. J., Van Wessem, J. M., Van Meijgaard, E., Van As, Di., Lenaerts, J. T. M.,
832 Lhermitte, S., Munneke, P. K., Smeets, C. J. P. P., Van Ulft, L. H., Van De Wal, R. S. W. and Van Den
833 Broeke, M. R.: Modelling the climate and surface mass balance of polar ice sheets using RACMO2 - Part 1:
834 Greenland (1958–2016), *Cryosphere*, 12(3), 811–831, doi:10.5194/tc-12-811-2018, 2018.
- 835 Nye, J. F.: Correction factor for accumulation measured by the thickness of the annual layers in an ice sheet,
836 *J. Glaciol.*, 4(36), 785–788, 1963.
- 837 Osterberg, E. C., Handley, M. J., Snead, S. B., Mayewski, P. A. and Kreutz, K. J.: Continuous ice core melter
838 system with discrete sampling for major ion, trace element, and stable isotope analyses, *Environ. Sci.
839 Technol.*, 40(10), 3355–3361, doi:10.1021/es052536w, 2006.
- 840 Osterberg, E. C., Hawley, R. L., Wong, G. J., Kopec, B., Ferris, D. and Howley, J.: Coastal ice-core record
841 of recent northwest Greenland temperature and sea-ice concentration, *J. Glaciol.*, 61(230), 1137–1146,
842 doi:10.3189/2015JoG15J054, 2015.
- 843 Overly, T. B., Hawley, R. L., Helm, V., Morris, E. M. and Chaudhary, R. N.: Greenland annual accumulation
844 along the EGIG line, 1959–2004, from ASIRAS airborne radar and neutron-probe density measurements,
845 *Cryosp.*, 10(4), 1679–1694, doi:10.5194/tc-10-1679-2016, 2016.
- 846 Polashenski, C. M., Courville, Z. R., Benson, C. S., Wagner, A., Chen, J., Wong, G. J., Hawley, R. L. and
847 Hall, D. K.: Observations of pronounced Greenland ice sheet firn warming and implications for runoff
848 production, *Geophys. Res. Lett.*, 41(12), 4238–4246, doi:10.1002/2014GL059806, 2014.
- 849 Reeves Eyre, J. E. J. and Zeng, X.: Evaluation of Greenland near surface air temperature datasets,



- 850 Cryosphere, 11(4), 1591–1605, doi:10.5194/tc-11-1591-2017, 2017.
- 851 Rennermalm, A. K., Moustafa, S. E., Mioduszewski, J., Chu, V. W., Forster, R. R., Hagedorn, B., Harper, J.
852 T., Mote, T. L., Robinson, D. A., Shuman, C. A., Smith, L. C. and Tedesco, M.: Understanding Greenland
853 ice sheet hydrology using an integrated multi-scale approach, Environ. Res. Lett., 8(1), 015017,
854 doi:10.1088/1748-9326/8/1/015017, 2013.
- 855 Rodriguez-Morales, F., Gogineni, S. P., Leuschen, C. J., Paden, J. D., Li, J., Lewis, C. C., Panzer, B., Gomez-
856 Garcia Alvestegui, D., Patel, A., Byers, K., Crowe, R., Player, K., Hale, R. D., Arnold, E. J., Smith, L.,
857 Gifford, C. M., Braaten, D. and Panton, C.: Advanced multifrequency radar instrumentation for polar
858 Research, IEEE Trans. Geosci. Remote Sens., 52(5), 2824–2842, doi:10.1109/TGRS.2013.2266415, 2014.
- 859 Sasgen, I., van den Broeke, M. R., Bamber, J. L., Rignot, E. J., Sorensen, L. S., Wouters, B., Martinec, Z.,
860 Velicogna, I. and Simonsen, S. B.: Timing and origin of recent regional ice-mass loss in Greenland, Earth
861 Planet. Sci. Lett., 333–334, 293–303, doi:10.1016/j.epsl.2012.03.033, 2012.
- 862 Selesnick, I. W. and Sidney Burrus, C.: Generalized digital butterworth filter design, IEEE Trans. Signal
863 Process., 46(6), 1688–1694, doi:10.1109/78.678493, 1998.
- 864 Serreze, M.: Northern Hemisphere cyclone locations and characteristics from NCEP/NCAR reanalysis data,
865 Verison 1, Natl. Snow Ice Data Center, Boulder, CO, Digit. media.[Available online <http://nsidc.org/data/nsidc-0423.html>], 2009.
- 867 Spikes, V. B., Hamilton, G. S., Arcene, S. A., Kaspari, S. and Mayewski, P. A.: Variability in accumulation
868 rates from GPR profiling on the West Antarctic plateau, Ann. Glaciol., 39, 238–244,
869 doi:10.3189/172756404781814393, 2004.
- 870 Steffen, K. and Box, J. E.: Surface climatology of the Greenland ice sheet : Overview of study area . Monthly
871 mean sea level pressure fields for (b) January , November the National Centers for Environmental
872 Prediction, J. Geophys. Res., 106(33), 951–964, doi:10.1029/2001JD900161, 2001.
- 873 Trusel, L. D., Das, S. B., Osman, M. B., Evans, M. J., Smith, B. E., Fettweis, X., McConnell, J. R., Noël, B.
874 and van den Broeke, M. R.: Nonlinear rise in Greenland runoff in response to post-industrial Arctic warming,
875 Nature, 564(7734), 104–108, doi:10.1038/s41586-018-0752-4, 2018.
- 876 Vandecrux, B., Fausto, R. S., Langen, P. L., Van As, D., MacFerrin, M., Colgan, W., Ingeman-Nielsen, T.,
877 Steffen, K., Jensen, N. S., Møller, M. T. and Box, J. E.: Drivers of Firn Density on the Greenland Ice Sheet
878 Revealed by Weather Station Observations and Modelling, J. Geophys. Res. Earth Surf.,
879 doi:10.1029/2017JF004597, 2018.
- 880 Vernon, C. L., Bamber, J. L., Box, J. E., Van Den Broeke, M. R., Fettweis, X., Hanna, E. and Huybrechts,
881 P.: Surface mass balance model intercomparison for the Greenland ice sheet, Cryosph., 7(5), 599–614,
882 doi:10.5194/tc-7-599-2013, 2013.
- 883 Wong, G. J., Hawley, R. L., Lutz, E. R. and Osterberg, E. C.: Trace-element and physical response to melt
884 percolation in Summit (Greenland) snow, Ann. Glaciol., 54(63), 52–62, doi:10.3189/2013aog63a602, 2013.
- 885 Wong, G. J., Osterberg, E. C., Hawley, R. L., Courville, Z. R., Ferris, D. G. and Howley, J.: Coast-to-interior
886 gradient in recent northwest Greenland precipitation trends (1952 – 2012), Environ. Res. Lett., 10(11),
887 114008, doi:10.1088/1748-9326/10/11/114008, 2015.
- 888 Yilmaz, Ö.: Seismic Data Analysis, Society of Exploration Geophysicists., 2001.
- 889 Zumberge, J. F., Heflin, M. B., Jefferson, D. C., Watkins, M. M. and Webb, F. H.: Precise point positioning
890 for the efficient and robust analysis of GPS data from large networks, J. Geophys. Res. Solid Earth, 102(B3),
891 5005–5017, doi:10.1029/96JB03860, 1997.
- 892